

OPEN ACCESS

EDITED BY Violante Di Donato, Unitelma Sapienza University, Italy

REVIEWED BY

Mutia Kehwalla Aza, The Johns Hopkins University, United States Zahra Sadat Dastgheib, Shiraz University of Medical Sciences, Iran

*CORRESPONDENCE
Xiaoyan Shi

☑ shixy019@sina.com

RECEIVED 11 July 2025 ACCEPTED 25 August 2025 PUBLISHED 12 September 2025

CITATION

Zhang S, Li T, Jiang D, Shi H, Hou H, Fu Z and Shi X (2025) Gold nanoparticles in the diagnosis and treatment of ovarian and cervical cancers: a comprehensive understanding. *Front. Oncol.* 15:1664340. doi: 10.3389/fonc.2025.1664340

COPYRIGHT

© 2025 Zhang, Li, Jiang, Shi, Hou, Fu and Shi. This is an open-access article distributed under the terms of the Creative Commons Attribution License (CC BY). The use, distribution or reproduction in other forums is permitted, provided the original author(s) and the copyright owner(s) are credited and that the original publication in this journal is cited, in accordance with accepted academic practice. No use, distribution or reproduction is permitted which does not comply with these terms.

Gold nanoparticles in the diagnosis and treatment of ovarian and cervical cancers: a comprehensive understanding

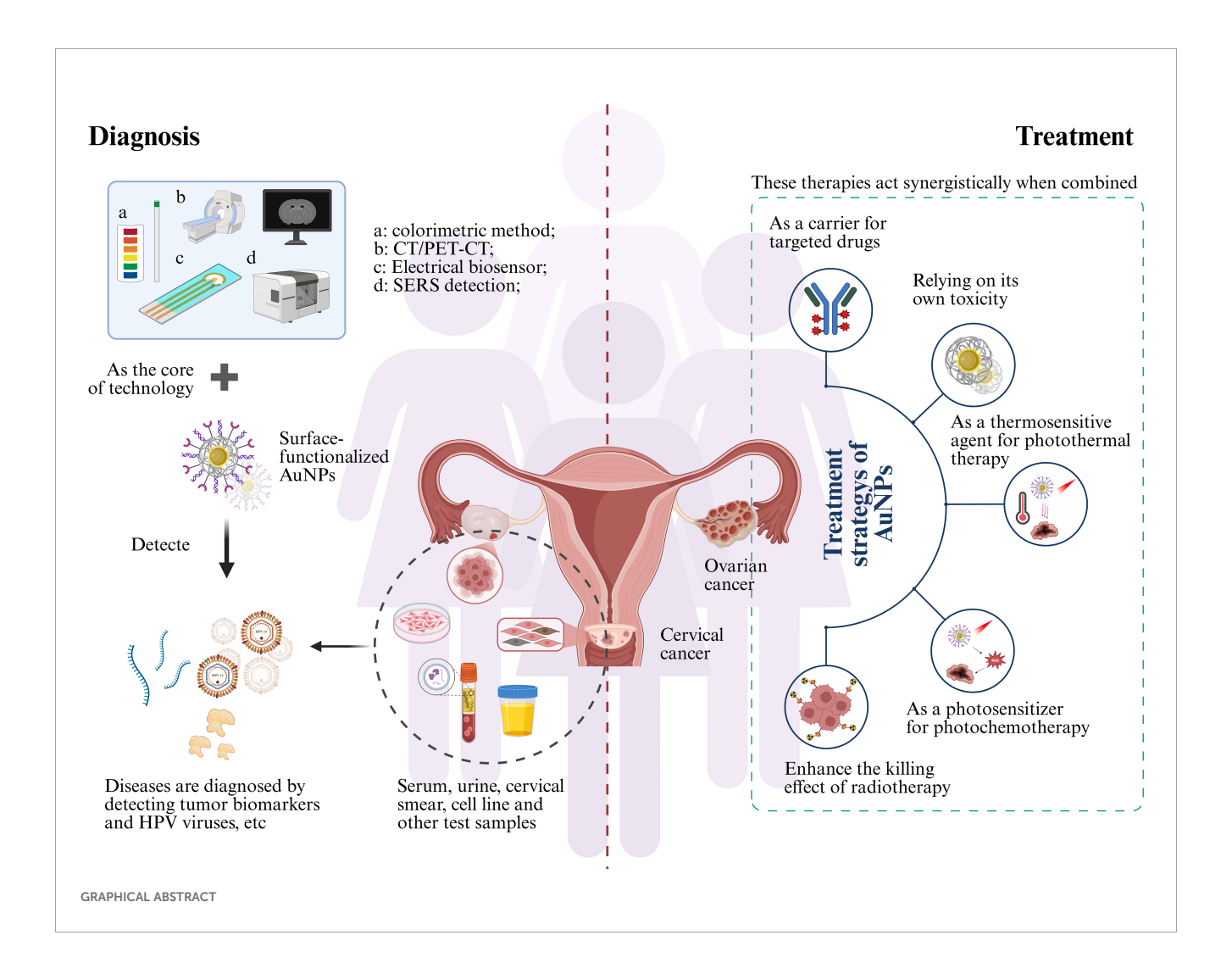
Senhui Zhang¹, Tong Li¹, Deshuo Jiang¹, Hengmei Shi¹, Huyang Hou¹, Ziyi Fu² and Xiaoyan Shi^{1*}

¹Department of Obstetrics and Gynecology, Women's Hospital of Nanjing Medical University, Nanjing Women and Children's Healthcare Hospital, Nanjing, China, ²Department of Breast Cancer Center, Affiliated Cancer Hospital of Nanjing Medical University, Jiangsu Cancer Hospital & Jiangsu Institute of Cancer Research, Nanjing, China

Cervical and ovarian cancers pose a significant global threat to women's health. Despite substantial medical advances in recent decades, gynecological malignancies remain a leading cause of female mortality, constrained by factors such as multidrug resistance, treatment toxicity, asymptomatic presentation in early stages, and genetic heterogeneity. Gold nanoparticles (AuNPs), leveraging their exceptional biocompatibility and multifunctional capabilities, demonstrate considerable potential across diverse fields including bioimaging, liquid biopsy, photothermal therapy, and targeted chemotherapy, thereby advancing precision oncology. Accordingly, this review synthesizes and analyzes the emerging applications of AuNPs in gynecological tumors over the past five years. Moving beyond superficial descriptions of functional features often limited in previous reviews, it places greater emphasis on elucidating the intrinsic relationships and mechanisms between functions from the perspective of their physicochemical properties. It further highlights the critical importance of AuNPs for constructing integrated diagnostic and therapeutic platforms. Simultaneously, this review provides a balanced examination of the challenges hindering the clinical translation of AuNPs and offers insights and perspectives on addressing these issues. It is anticipated that AuNPs may evolve into highly effective diagnostic and therapeutic strategies in the future.

KEYWORDS

gynecological malignant tumors, cervical cancer, ovarian cancer, nanotechnology, gold nanoparticles, diagnosis, treatment



1 Introduction

Cervical and ovarian cancers represent the most lethal gynecological malignancies, each posing distinct clinical challenges. HPV infection constitutes the primary etiological factor for most cervical carcinomas, thus establishing HPV testing as critical for early screening (1). Organized screening and HPV vaccination provide key prevention strategies, especially in developing nations (2). The protracted asymptomatic latency spanning decades from cervical intraepithelial neoplasia to invasive carcinoma creates significant fertility preservation challenges for reproductive-aged patients, given that radical hysterectomy remain primary therapeutic options (3, 4). Ovarian cancer demonstrates the highest aggressiveness among gynecological malignancies, with its characteristically asymptomatic early-stage presentation resulting in fewer than 50% of patients surviving beyond five years post-diagnosis (5, 6). Molecular heterogeneity, intrinsic chemoresistance, and rapid metastatic dissemination collectively contribute to its elevated mortality (7).

Conventional strategies lack early precision and fail to prevent multidrug resistance, necessitating advanced approaches (8, 9). With advancements in oncology, nanotechnology has emerged as a promising frontier (10, 11). Therapeutically, multifunctional

nanoparticle-based drug delivery platforms enable cancer cell-specific targeting while sparing healthy tissues, thereby reducing systemic drug exposure, minimizing toxicity, and delaying resistance emergence (12–14). Diagnostically, nanoparticles enhance tumor biomarker detection sensitivity, facilitating earlier clinical intervention (15, 16).

Among diverse nanomaterials, gold nanoparticles (AuNPs) stand out due to exceptional biocompatibility and their defining optical property (17). AuNPs are synthesized through established methods including the Turkevich citrate reduction, biological synthesis using plant/microbial extracts, and physical approaches like laser ablation, enabling precise control over size, morphology, and surface functionalization for biomedical applications (18). Localized Surface Plasmon Resonance (LSPR) arises from collective electron oscillations, generating intense, tunable absorption/scattering for colorimetric sensing and enabling Surface-enhanced Raman scattering (SERS) via electromagnetic "hot spots" for trace analyte detection (19, 20). Critically, LSPR drives efficient light-to-energy conversion, underpinning AuNPs' efficacy as potent photothermal agents and photosensitizers in photothermal therapy (PTT) and photodynamic therapy (PDT) (21). As the morphology progressively evolves, AuNPs' amplified surface-area-to-volume ratio enhances biomolecular

interactions, while exceptional electrical conductivity (>10⁵ S/m for 20-nm particles) facilitates ultrasensitive detection (18, 22, 23). LSPR "hot spots" also modulate fluorescence and enable fluorescence resonance energy transfer (FRET) (24).

AuNPs' surfaces are readily functionalized via covalent conjugation, biomolecular assembly, or polymeric encapsulation (e.g., thiol anchoring, amide bonds, click chemistry, electrostatic adsorption) to confer targeting specificity, colloidal stability, and multifunctionality (25, 26). This enables active targeting (antibodies/peptides/aptamers) (27) or passive magnetic guidance (Fe₃O₄ composites) (28), allowing their use as multimodal contrast agents (MRI/X-ray/OCT) (29). Furthermore, AuNPs exhibit distinct catalytic activity in redox reactions, enabling applications in electrochemical biosensors (30). Collectively, these physicochemical properties underpin AuNPs' transformative potential in diagnosing and treating gynecological malignancies.

Collectively, AuNPs represent a pivotal milestone in precision medicine, offering transformative potential for timely cancer intervention. The following sections detail the application of AuNPs, critically evaluating their contributions to diagnosing and treating gynecological malignancies to establish a reference framework for clinical practice.

2 AuNPs in cervical cancer

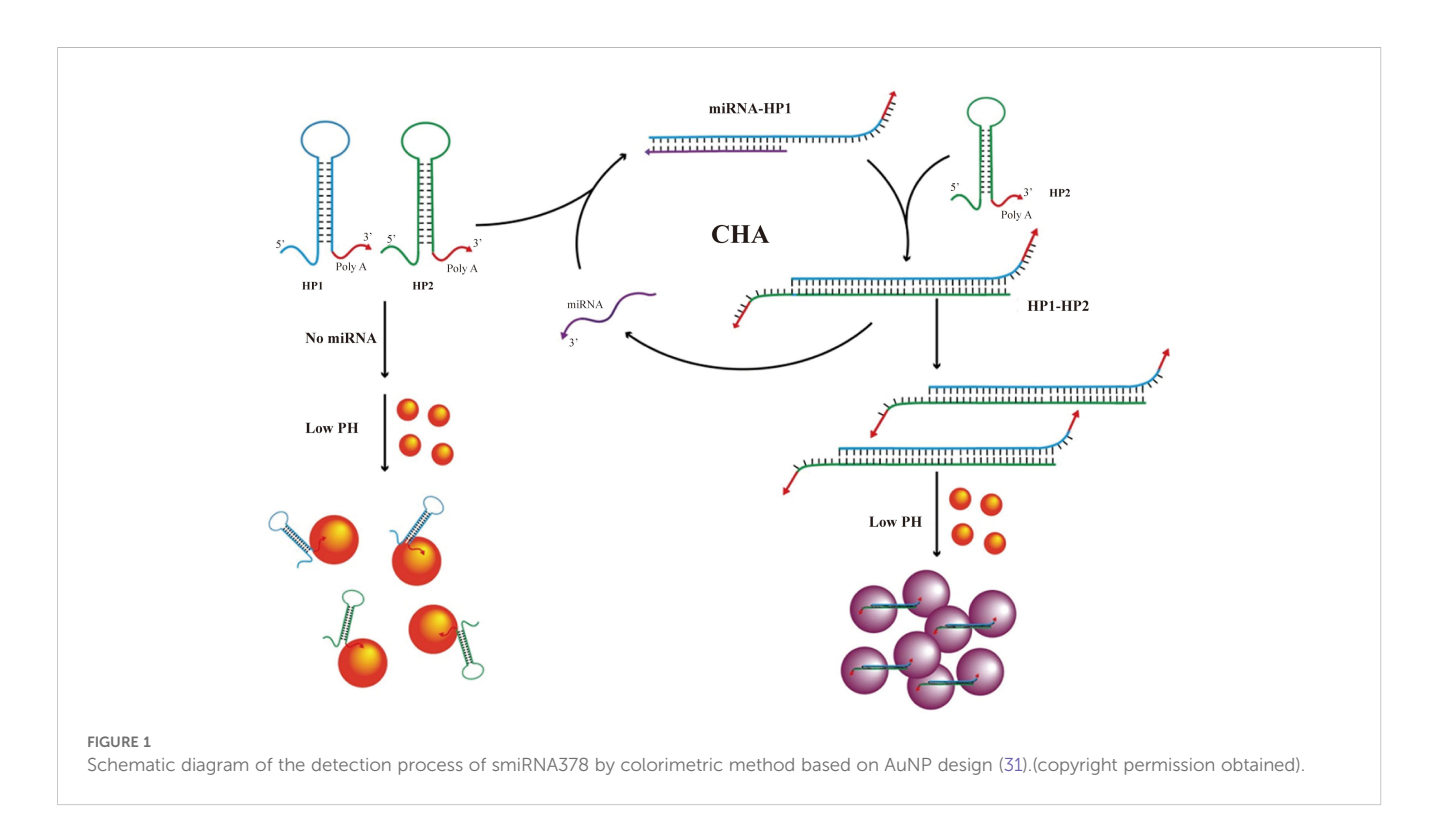
2.1 Diagnosis

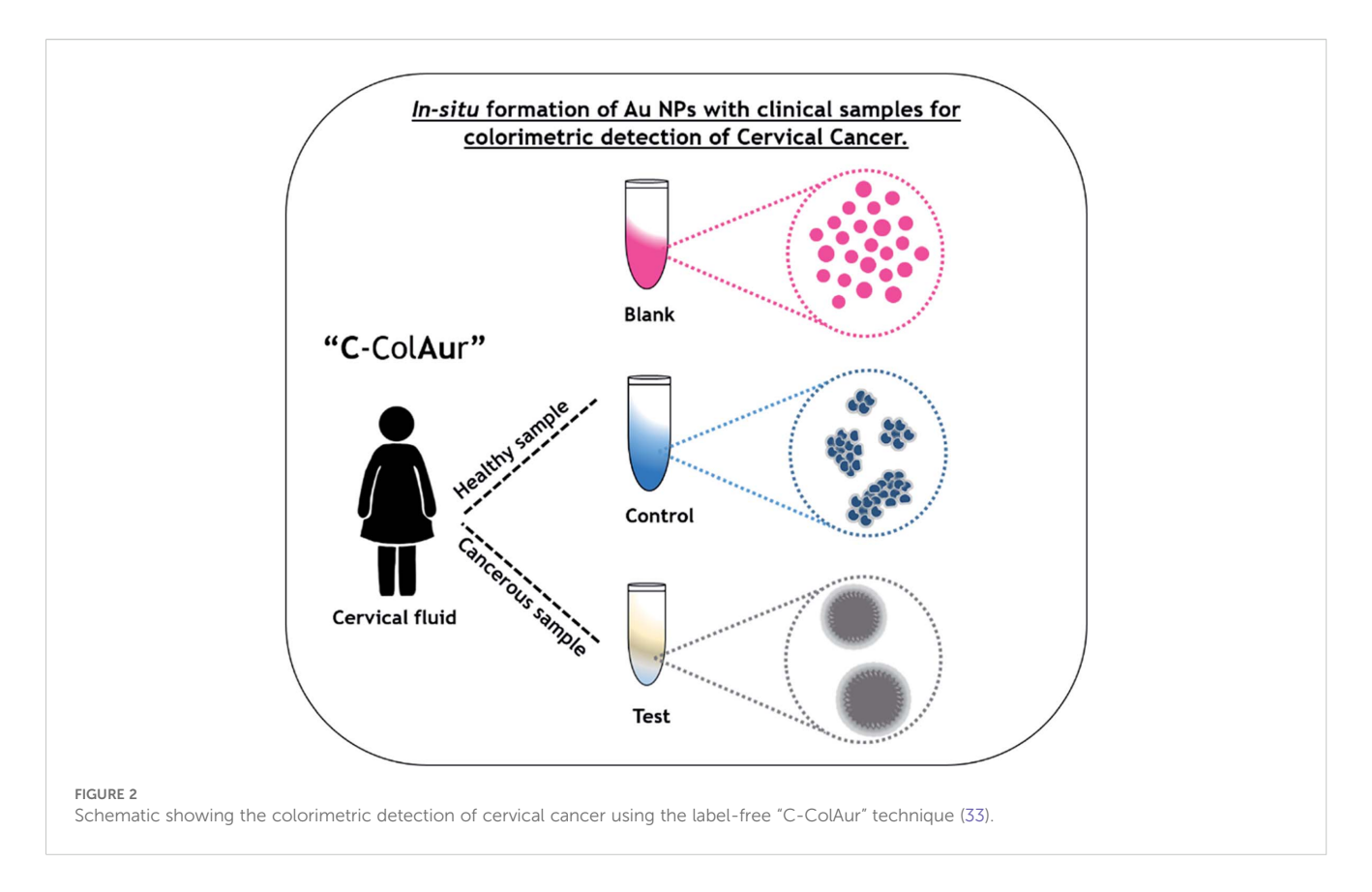
2.1.1 Colorimetric detection utilizing AuNPs

Functionalized AuNPs undergo LSPR peak shifts and visible color changes upon binding target molecules. AuNPs-based

colorimetric assays thus exploit this phenomenon to assess levels of cervical cancer biomarkers through readily observable color transitions (31). microRNA-378 is consistently dysregulated in cervical cancer. Run and colleagues developed a colorimetric assay using catalytic hairpin assembly (CHA) and AuNPs for its detection (31). Target miRNA-378 triggers CHA between two hairpin probes, generating polymeric products. Multiple polyadenine blocks on these products adsorb and cross-link AuNPs (~13nm, Citrate-reduced) under acidic conditions, inducing aggregation. This shifts the LSPR, causing a visible color change from red to purple (Figure 1) (31). The assay leverages nucleic acid hybridization specificity, offering operational simplicity, high sensitivity, and strong specificity, with a LOD of 20.7 pM (31).

Motivated by the high cost of target-specific AuNP functionalization, label-free C-ColAur was developed as an alternative (32). Label-free C-ColAur is a nonspecific detection method leveraging AuNPs color shifts from LSPR. Target binding protects AuNPs from salt-induced aggregation, enabling rapid onsite pathogen screening via visible color changes, particularly in resource-limited settings (32). Applied to cervicovaginal fluid, it shows distinct color changes: AuNPs turn blue in healthy samples but remain unchanged in cancer samples, achieving high diagnostic accuracy (96% sensitivity, 87% specificity; Figure 2) (33). Transmission Electron Microscope (TEM) revealed significantly larger AuNP diameters (250~400nm, Citrate-reduced, Quasi-Spherical) in patients versus controls (15~30nm, Citrate-reduced, Quasi-Spherical), with reduced particle numbers and absence of aggregation in cancer samples (33). Tejaswini et al. proposed that cancer cell membrane components induce aggregation (34). Experimental validation confirmed that synthetic lipids, but not proteins or lipid-protein mixtures, replicated the color or spectral





shift when reacted with HAuCl₄·3H₂O and ascorbic acid, indicating lipid-specific organization drives the mechanism (34).

HR-HPV is the primary cause of cervical cancer. Conventional detection (qPCR, isothermal amplification, dot blot) faces limitations including contamination risk, incomplete subtyping, and high cost (35). AuNP-based colorimetric assays (57.7 ± 4.2nm, Citrate-reduced, Quasi-spherical with dendritic protrusions) enable instrument-free, visual or smartphone-based readout of HPV-16/18, permitting quantitative results acquisition by untrained personnel without specialized equipmen (36). Carlos conjugated AuNPs (21.6 ± 0.1nm, Turkevich) with anti-HPV-16/18 L1 antibodies (37). Applied to 173 cervical samples, infection caused a color shift(red to purple) and LSPR red-shift (523~525 nm to 524~590 nm) (37). The assay detected HPV-16 L1 (linear range: 0.4~2.0µg/mL, LOD: 0.18µg/mL) and HPV-18 L1 (0.2~1.2µg/mL), identifying PCR-missed variants potentially via conserved L1 epitope recognition (37). To expand coverage, Jixue and team developed a multiplexed closed-tube PCR, detecting 17 HPV types (LOD: 0.5copies/µL, linear range: 0~1000copies/µL) with 99.05% accuracy (38).

2.1.2 AuNPs-engineered electrochemical biosensors

Colorimetry lacks micro-scale sensitivity. Electrochemical biosensors convert biorecognition events to electrical signals (39). CEA, SCCA, Ki67, p53, and p16 $^{\rm INK4a}$ are key cervical cancer biomarkers (35). Antibody-conjugated AuNPs enable their multiplexed detection. Electrochemical sensors universally use: 1) conductive substrates (Pt/Co/MoS₂/WS₂/rGO) to amplify AuNPs

signals, and 2) engineered porous architectures (SiO₂ dendrimers, multilayered nanoparticles, 3D networks) to enhance target capture and conductivity (Table 1) (40-42). These AuNPs-centered platforms show diagnostic promise (40). In a recent study, Hiranmoy et al. developed an ultrasensitive electrochemical immunosensor for cervical cancer biomarker $p16^{\mathrm{INK4a}}$ detection by modifying a glassy carbon electrode through sequential deposition of graphene oxide and ~70nm spherical AuNPs (43). The sensor utilized cysteamine-glutaraldehyde crosslinking to immobilize p16^{INK4a} monoclonal antibodies on the electrode surface (43). Compared to bare electrodes, Au/rGO-modified electrodes exhibited significantly enhanced peak currents with charge transfer resistance (Rct) reduced from 245 Ω to 14 Ω , demonstrating AuNPs' capacity to facilitate electron transfer. Clinical serum analysis via square wave voltammetry achieved 100% accuracy with a detection limit of 167 fg/mL and linear range from 500 fg/mL to 100 ng/mL (43). The AuNP-engineered sensor demonstrated exceptional selectivity, storage stability, repeatability, reproducibility and regeneration capability.

Similarly, while colorimetry detects cervical exfoliated cells, its accuracy suffers from subjective visual interpretation of subtle color shifts. AuNP-integrated (~16nm, Citrate-reduced, Spherical, chitosan-coated) photoelectric sensors enhance precision by targeting cancer-specific α2,6-sialic acid overexpression via SNA-conjugated AuNPs (44). Ricardo and team detected diagnostic spectral alterations at 1470, 1456, 1434, 1400, and 1350 cm⁻¹ in cancer-bound complexes using attenuated total reflection fourier-transform infrared spectroscopy (ATR-FTIR) (44). Notably,

Ricardo et al. leveraged machine learning (ML), specifically principal component analysis (PCA), to identify sialic acid-associated spectral signatures in cervical cancer cell lines. Orthogonal principal components maximizing data variance were derived, enabling construction of confidence ellipse models that robustly discriminated primary fibroblasts from malignant cells (non-overlapping 95% confidence intervals; p<0.001) (44). This approach establishes a non-invasive diagnostic paradigm for early cervical cancer detection through surface-enhanced infrared absorption (SEIRA) biomarker profiling. (Figure 3).

AuNPs enhance HPV-16 DNA detection by increasing electrode surface area, accelerating electron transfer, and amplifying signals (39, 45). As Table 2 shows, varied electrode designs achieve LODs<0.2fM (46-49). Dielectric and photoelectrochemical sensors offer enhanced precision, with maintained functionality during long-term cold storage (46, 48).

Lin and colleagues' paper-based sensor achieves significant cost reduction (<\$1.00), miniaturization, and commercial viability (53). Utilizing lateral flow principles, HPV-16/18 DNA hybridizes with probes in a rapid-flow zone, forming circular structures that bind AuNPs (~40nm, Spherical)-polydopamine (PDA). Light irradiation triggers AuNP-mediated photothermal conversion, intensifying thermal response while diminishing photocurrent. Subsequent fluid migration to a slow-flow zone enables CRISPR-Cas12amediated DNA cleavage and HPV fragment release, reversing signals (Figure 4) (53). This system detects HPV-16/18 DNA within 30 minutes with high specificity (LOD: 0.21pM and 42.92pM, respectively) (53). However, Lin's sensor is susceptible to temperature, salt concentration, and reaction time variations due to pre-hybridization nucleic acid cleavage. These factors exacerbate electrical signal transduction limitations, including single-molecule counting inability. To overcome this, Jia and team integrated darkfield microscopy (DFM) imaging, circumventing signal dependency while employing synergistic sedimentation (SynSed) to minimize nanoparticle diffusion (~15nm, Citrate-reduced) (54). This optimized system achieves a LOD of 10 fM.

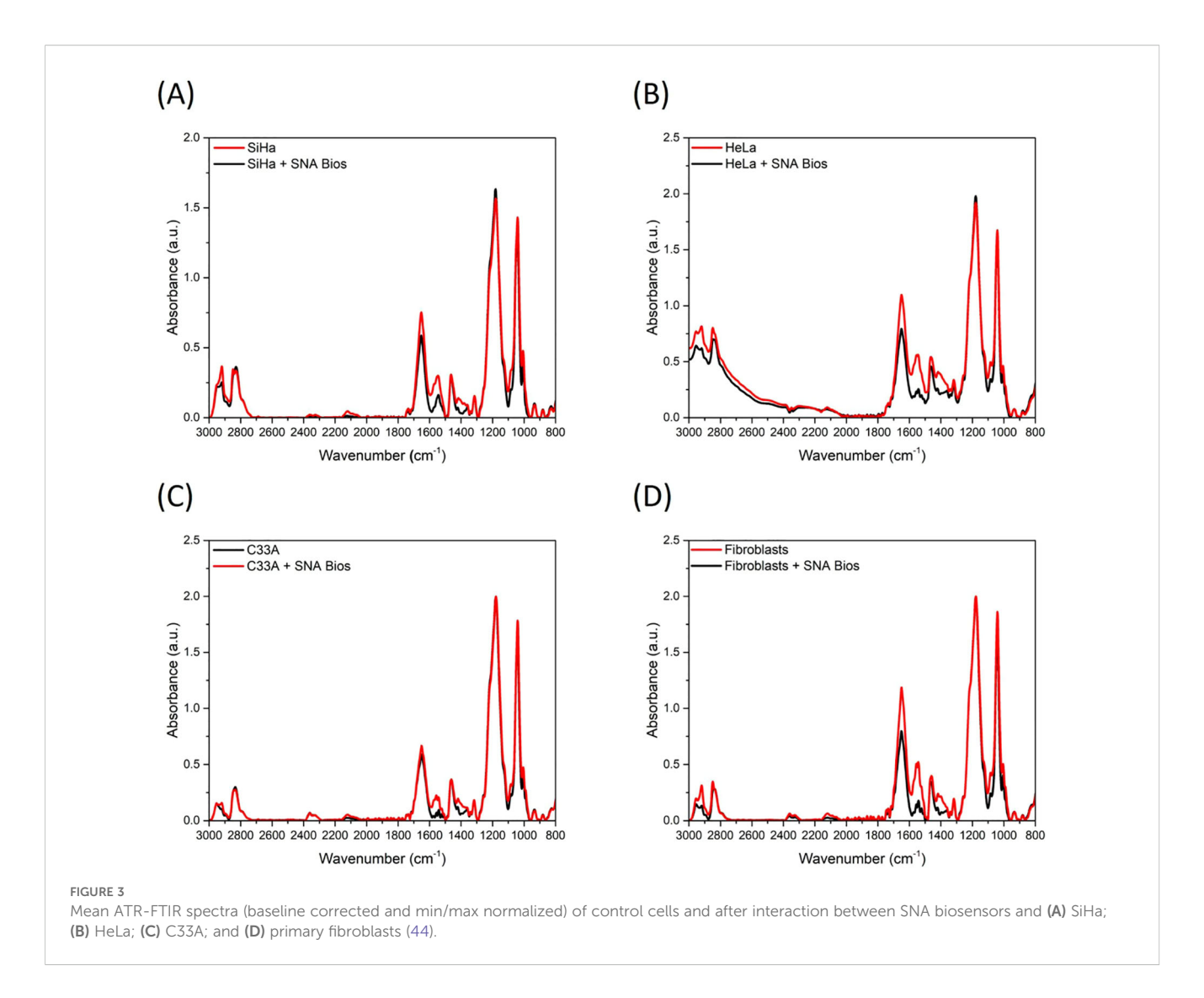
Beyond HPV-16 and HPV-18, other high-risk HPV types (31, 56, 59, 68) also contribute to cervical cancer development (35). To address this, platforms incorporating MY11 probes targeting conserved regions of the HPV L1 gene have been integrated with AuNPs-doped detection systems. AuNPs amplify current-voltammetric signals generated by minor nucleotide variations within the L1 conserved regions of HPV-16/31/33/45/58, enabling the construction of HPV genotyping profiles (51). Conversely, an alternative strategy anchors multiple recognition probes within a photoelectrochemical biochip array (PEBA) platform composed of TiO₂@AuNPs composites (52). This highly integrated chip-based format achieves an exceptionally low LOD of 0.1 copies/μL, demonstrating high concordance with clinical results (52).

2.1.3 SERS detection based on AuNPs

SERS surpasses electrochemical biosensors in AuNPs-based serological diagnostics by circumventing electrode constraints. As Table 3 shows, platforms utilize: 1) sharpened AuNPs geometries to intensify electromagnetic hotspots, and 2) ordered array chips to

TABLE 1 Research on the detection of serum tumor markers.

9 2	Particle size Targe	Targe	Surface functionalization	Highlights of Study	Clinical sample LOD	ГОР	Linear range	Reference
	317.4 ± 12.3nm	miRNA-21	Thiolation	MoS ₂ /AuNPs composite-modified electrode and multilayered nanoneedle structure	Artificial serum	38aM	10aM~1uM	(41)
2	ı	SCCA	Thiolation	Bimetallic PtCo nanoframe-modified electrode and dendritic DM-SiO $_2$ @AuPt core-shell nanostructures	Artificial serum	7.33fM	22.22fM~2.67µM	(42)
8	13.2 ± 2.32nm	p16 ^{INK4a} , P53; Ki67	Thiolation; Electrostatic adsorption	Schematic of label-free sensing with redox reporters (Cd²+/DAP/MB);3SPCE array/GO/2D WS₂/PEI-AuNPs/redox probe	Artificial serum	9.38nM; 5.49nM; 0.56nM	0.01~100ng/mL	(40)
4	~16nm	α2, 6-sialic acid	Electrostatic adsorption	ATR-FTIR combined with chemometrics for biosensor-cell interaction signal enhancement.	I	I	I	(44)
2	~75nm	p16 ^{INK4a}	Thiolation	The Au-rGO material was employed for the first time to detect serum $p_1 6^{\rm INK4a}$.	serum(15)	167fg/mL	500fg/mL~100ng/mL (43)	(43)



enhance spectral reproducibility (55–58). However, significant LOD variability exists (e.g., 191.73 fM vs. 10 fM for SCCA in serum) (55, 58), likely stemming from AuNPs morphology and Raman reporter differences (Figure 5).

SERS and Surface Plasmon Resonance Imaging (SPRi) are increasingly favored for cervical cancer biomarker detection (Table 3). Yifan and team developed a dual-mode SPRi/SERS biosensor with a polyA capture probe/target miRNA/AuNPs-enhanced probe sandwich architecture (60). This platform concurrently detects miRNA-21/124/143 on a single chip (60). Target hybridization forms ternary complexes where AuNPs enhance SPRi via refractive index modulation while generating SERS hotspots through LSPR (60). Dual-signal redundancy reduces false positives (serum recovery: 90.0–100.2%) (60). This high-throughput platform provides dual-verified nucleic acid detection with clinical utility.

The spatial arrangement of AuNPs in SERS sensors critically determines analytical outcomes. Xingkang et al. engineered a nanoscale monolayer film of uniform AuNPs (83 ± 6nm) to generate evenly distributed dense hotspots, overcoming the random hotspot distribution characteristic of conventional

plasmonic colloidal solutions (64). This design prevented heterogeneous electromagnetic signals arising from nanoparticle aggregation while enhancing SERS signal reproducibility and sensitivity (64). Furthermore, integration of CD63 nanoflares with AuNPs created supplemental hotspots that amplified SERS intensity by 4.1-fold (64). The resulting platform exhibited linear detection of cancer exosomes from 1×10^6 to 2×10^8 particles/mL with a limit of detection (LOD) of 4.7×10^5 particles/mL (64).

Artificial intelligence enables more efficient mining of the massive data generated by AuNP probes in SERS sensing analysis, forming the foundation for low-cost nonspecific analysis. Hongmei and team established that 10 ppm serum prevents AuNPs encapsulation while enhancing dispersion homogeneity (63). After screening lasers, they selected 785 nm and 633 nm excitation (excluding 532 nm due to fluorescence interference), achieving 0.9609 spectral cosine similarity at 10 ppm (63). Clinical validation with 36 sera (24 healthy/12 cancer) identified differential peaks at 1201 cm⁻¹ and 1312 cm⁻¹. PCA achieved complete group separation, establishing the first standardized SERS reference library for cervical cancer sera. This methodology provides a robust foundation for clinical SERS translation (63).

Zhang et al.

TABLE 2 Recent advances in HPV detection biosensors.

No	Particle size	Targe	Surface functionalization of AuNPs	Highlights of Study	Clinical sample	LOD	Linear range	Reference
1	-	HPV 16 DNA	-	Exhibits strong anti-interference capability in human serum	Artificial serum	0.5475 fM	100fM~1000nM	(50)
2	-	HPV-18 DNA	Thiolation	rGO-MWCNT-AuNPs nanocomposite-functionalized SPCEs	Cervical smear	0.05fM	0.01fM~0.01nM	(47)
3	16 ± 1nm	HPV-16 DNA	Thiolation	APTES-modified GCE; CP-AuNPs immobilized via phosphate- amine electrostatic adsorption	Artificial serum	0.1731fM	100fM~10uM	(46)
4	18.9 ± 1.5nm	HPV-16 E6/E7 mRNA	Thiolation; Covalent bonding	LAMP-amplified mRNA; Streptavidin modification; ssDNA- AuNPs targeting; SA-HRP signal amplification	Cervical smear(20)	0.08fM	100nM~100uM	(48)
5	-	HPV L1	Electrostatic adsorption	PANI electrode with AuNPs deposition; MY11 degenerate probe	Cervical smear	0.113nM	1~100 pg/μL	(51)
6	~5nm	HPVs	-	Screen-printed photoelectrode array modified with TiO ₂ @AuNPs	Positive cervical smear(20); negative cervical smear(20)	0.1copies/μL	0.6~600copies/μL	(52)
7	9 ± 1.5nm	HPV-18 DNA	Covalent bonding	${ m SiO_2} ext{-micro-IDE}$ substrate; APTES-AuNPs dehydration-condensation modification	Cervical smear(20)	0.529aM	1aM~100fM	(49)
8	~40nm	HPV-16/18 DNA	Electrostatic adsorption	CuCo ₂ S ₄ -ZnIn ₂ S ₄ -S heterojunction interface; Paper-film composite chip	Serum	0.21pM; 42.92pM	-	(53)
9	~15nm	HPV-16	-	Using SynSed technology as an alternative method for particle transfer in DFM imaging	Artificial serum	10fM	0pM~500pM	(54)
10	~50nm	HPV-16	Covalent bonding	This is the first dual-colorimetric strategy based on AuNPs for detecting double-stranded HPV-16 viral genome.	Cervical smear	1.9nM	0.45~6.72nM	(45)

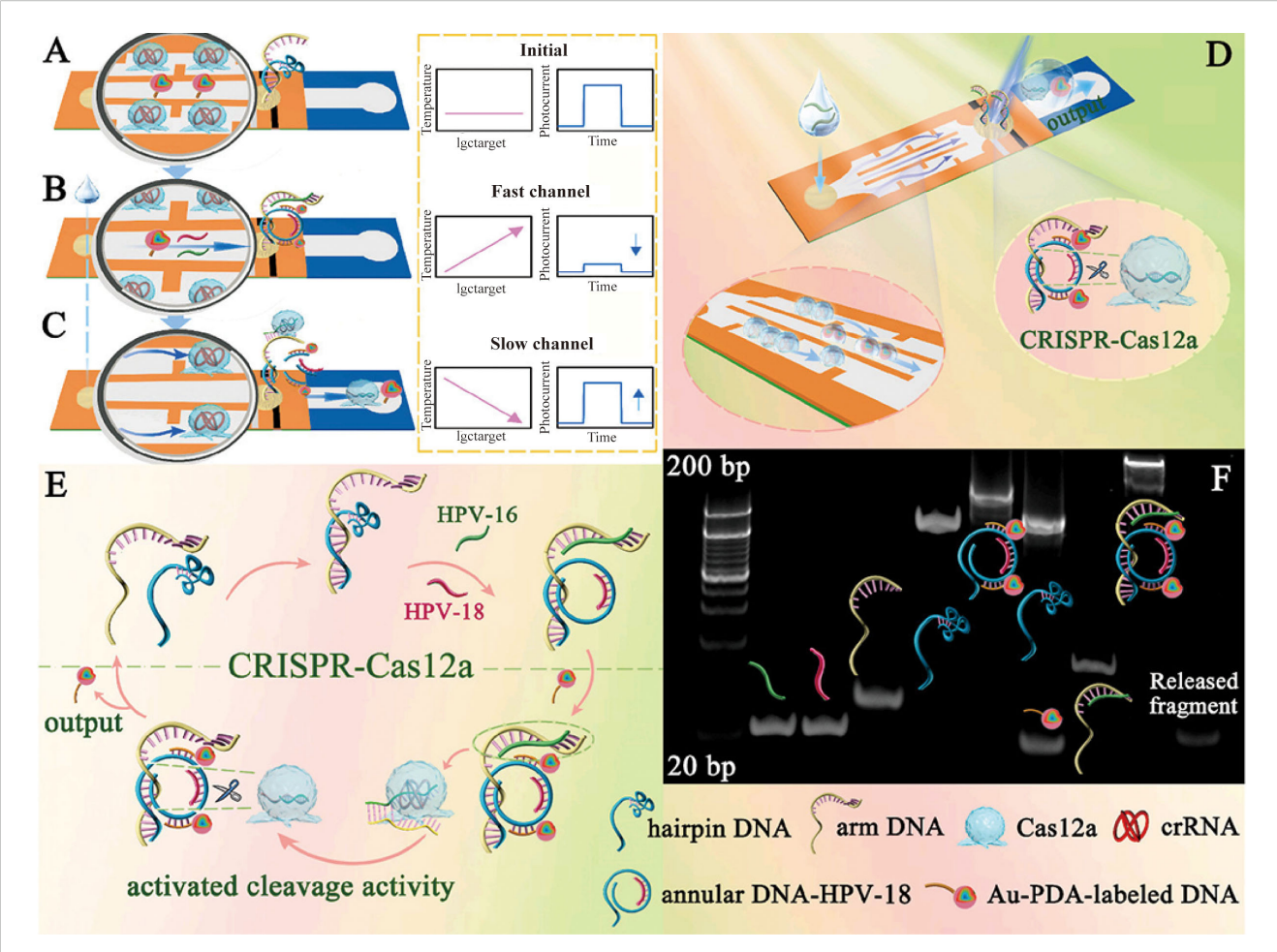


FIGURE 4
Detection steps and interactive signal change process in the (A) initial state, (B) the DNA conformational change state, and (C) CRISPR-Cas12a activation state. (D) Schematic diagram of the proposed lateral flow biosensor. (E) Signal amplification process of the CRISPR-Cas12a-driven dual-readout lateral flow biosensor. (F) Feasibility analysis for the self-assembly process of the annular DNA and trans-cleavage instinct of CRISPR-Cas12a (53). (copyright permission obtained).

Meanwhile, this simultaneously enables unsupervised recognition of cervical cell pathology through AI analysis of non-functionalized gold nanoparticles (nfGNPs). Karunakaran et al. implemented support vector machine (SVM) algorithms to achieve highprecision classification of NRML/HSIL/CSCC specimens (94% ± 0.73% accuracy for single-cell analysis), markedly improving post-PCA specificity with ROC-validated diagnostic progression (AUC >0.98) for cervical lesion stratification (61). In contrast, Diao et al. adopted a PCA-LDA fusion strategy (62). Following Savitzky-Golay filtering with airPLS background correction and min-max normalization, PCA reduced spectral dimensions to 46 principal components retaining 95% of the variance (62). LDA then compressed these into two discriminative factors. This hierarchical approach resolved non-overlapping 95% confidence ellipses observed under singular methods and attained 91.1% accuracy in differentiating exosomes across H8, HeLa, and MCF-7 cell lines (62). The model demonstrated robust diagnostic efficacy, with AUCs ranging from 0.93 to 0.99, and maintained 93.3% overall accuracy in clinical validation (62). It perfectly classified breast and cervical cancer serum exosomes while correctly identifying 80% of

healthy samples. This established a non-invasive framework for SERS-driven early cancer detection (62).

2.1.4 AuNPs-enabled innovative imaging strategies

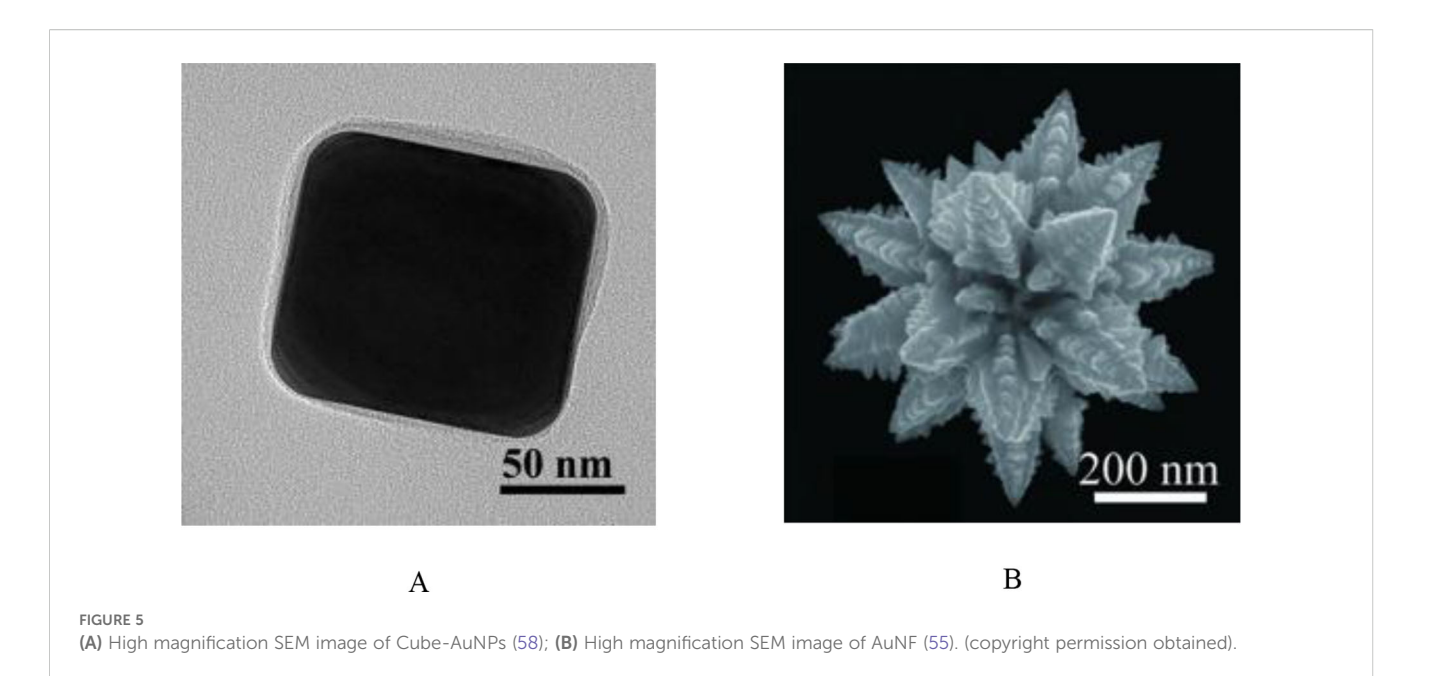
Imaging is vital for non-invasive cervical cancer diagnosis. Tumor-targeting ligand-functionalized AuNPs (e.g., folic acid, oligotyrosine/RGD/NLS peptides) serve as effective contrast agents (65). The tumor microenvironment further enhances AuNPs (50.3 \pm 1.1nm, Citrate-reduced, spherical) accumulation, where acidic pH triggers hydrolysis of citraconic anhydride linkages in AuNPs-doxorubicin (DOX) complexes (66).

Radioiodinated AuNPs serve as contrast agents for clinical imaging (MRI/US/CT/PET) (29). Min and colleagues engineered pH-responsive theranostic AuNPs (50.3 ± 1.1nm, Microwave-assisted synthesis, spherical) with PEGylated surfaces and citraconic anhydride-linked DOX (66). At pH 5.5, linker hydrolysis triggers DOX release and electrostatic aggregation (35-nm UV-Vis redshift; TEM-confirmed), amplifying imaging signals (66). Radioiodination achieved 35.4% labeling efficiency, with PET showing 1.37%ID/g

Zhang et al.

TABLE 3 Research on the detection of cervical cancer (SERS).

No	Particle size	Targe	Surface functionalization of AuNPs	Highlights of Study	Clinical sample	LOD	Linear range	Reference
1	~600nm	SCCA; OPN	-	Ag-AuNFs bimetallic nanocomposites with arrow- headed tip nanostructures	Serum(150)	191.73fM; 132.97fM	10 pg/mL~9 μg/mL	(55)
2	~45nm	В7-Н6	Covalent bonding	Zwitterion-modified stealth sensor with pH-stable spiky AuNPs	Positive serum(9); negative serum(1)	10fM	10fM~10nM	(56)
3	~20nm	CpG methyltransferase	-	Site-selective assembly of AuNP arrays on monolayer SiO ₂ arrays yielding Au@SiO ₂ array substrates;RCA signal amplification strategy	Serum(150)	0.251mU/mL	0.005~50U/mL	(57)
4	~20nm	SCCA; CEA	-	Cubic Ag-Au bimetallic nanoparticles integrated on Au@SiO ₂ array substrates;Pump-free flow via capillary pump/hydrophilic-treated channels;Multichannel parallel auto-detection	Positive serum(60); negative serum(30)	10fM; 2fM	1pg/mL~1μg/mL	(58)
5	70~80nm	p16;Ki-67	Covalent bonding	AuNS@Ag nanoflowers enable 20-min slide detection, bypassing ICC staining.	Cervical smear	-	-	(59)
6	~20nm	miRNA21/124/143	-	SPRi: AuNP-helper probes enhance chip signals; SERS: Triplex Raman reporters hybridize with target miRNAs.	-	1 fM; 0.8 fM; 1.2 fM	10 fM~100pM	(60)
7	40~45nm	-	-	SERS on single cells/spheroids/DNA + chemometrics (PCA/LDA/SVM) for cervical cancer detection; validated by cytology/HPV PCR/UFLC metabolomics.	Cervical smear	-	-	(61)
8	~80nm	-	-	"Hotspot"-rich 3D plasmonic AuNP-nanomembranes: LLISA-assembled monolayers triple-stacked on ITO; optimized with AI.	Positive serum(12); negative serum(5)	-	-	(62)
9	~25nm	-	-	A reliable detection protocol was established to obtain highly stable and reproducible serum SERS spectra	Positive serum(12); negative serum(24)	-	-	(63)
10	83 ± 6nm	sEV	-	Detection of cancerous exosomes using plasmonic AuNPs nanosheets as SERS substrates combined with CD63 nanoflares	Positive serum(11); negative serum(8)	4.7×10^5 particles/mL.	$1 \times 10^6 \sim 2 \times 10^8$ particles/mL	(64)



tumor uptake at 2h and >38% cancer cell binding (66). Photoacoustic imaging (PAI) generates biological images by detecting photon emissions from contrast agents. AuNPs exhibit exceptional PAI properties due to high photothermal conversion efficiency (66). The Au-UCNP-PEG_{2k} nanocomposite serves as both photodynamic therapy agent and multimodal imaging platform (~5nm, Hydrothermal method, spherical) (67). *In vivo* studies show superior PAI performance under near-infrared region (NIR) irradiation compared to bare AuNPs, functioning as a trimodal contrast agent for comprehensive tumor diagnostics (Figure 6) (67).

AuNPs enhance lesion identification in laboratory imaging (68). Under DFM, FA-targeted AuNPs@Ag@AgI nanostructures internalized by HeLa cells enable precise spatial localization via amplified light scattering (68). Simultaneously, AuNPs' plasmonic properties mediate surface energy transfer to fluorescent donors (e.g., TAP, PHEN), inducing controlled fluorescence quenching within cells, supporting development of real-time imaging agents (68).

2.2 Treatment

2 .2.1. AuNPs-based drug delivery systems

AuNPs enable targeted cancer cell eradication via drug and ligand conjugation. Therapeutic payloads encompass Methotrexate (MTX) (69), DOX (66), Paclitaxel (PTX) (70), and luteolin (71). Common cervical cancer targeting ligands comprise Folic Acid (FA), Hyaluronic Acid (HA), and AS1411 aptamer (Table 4). Emerging agents show complementary potential (72). The investigational compound IQ activates TLR7/8-mediated immune responses and NF-κB-dependent apoptosis. When complexed with nucleolintargeting AS1411 aptamer on AuNPs (IQ-AS1411-AuNPs), MTT assays demonstrated significantly reduced HeLa cell viability (72).

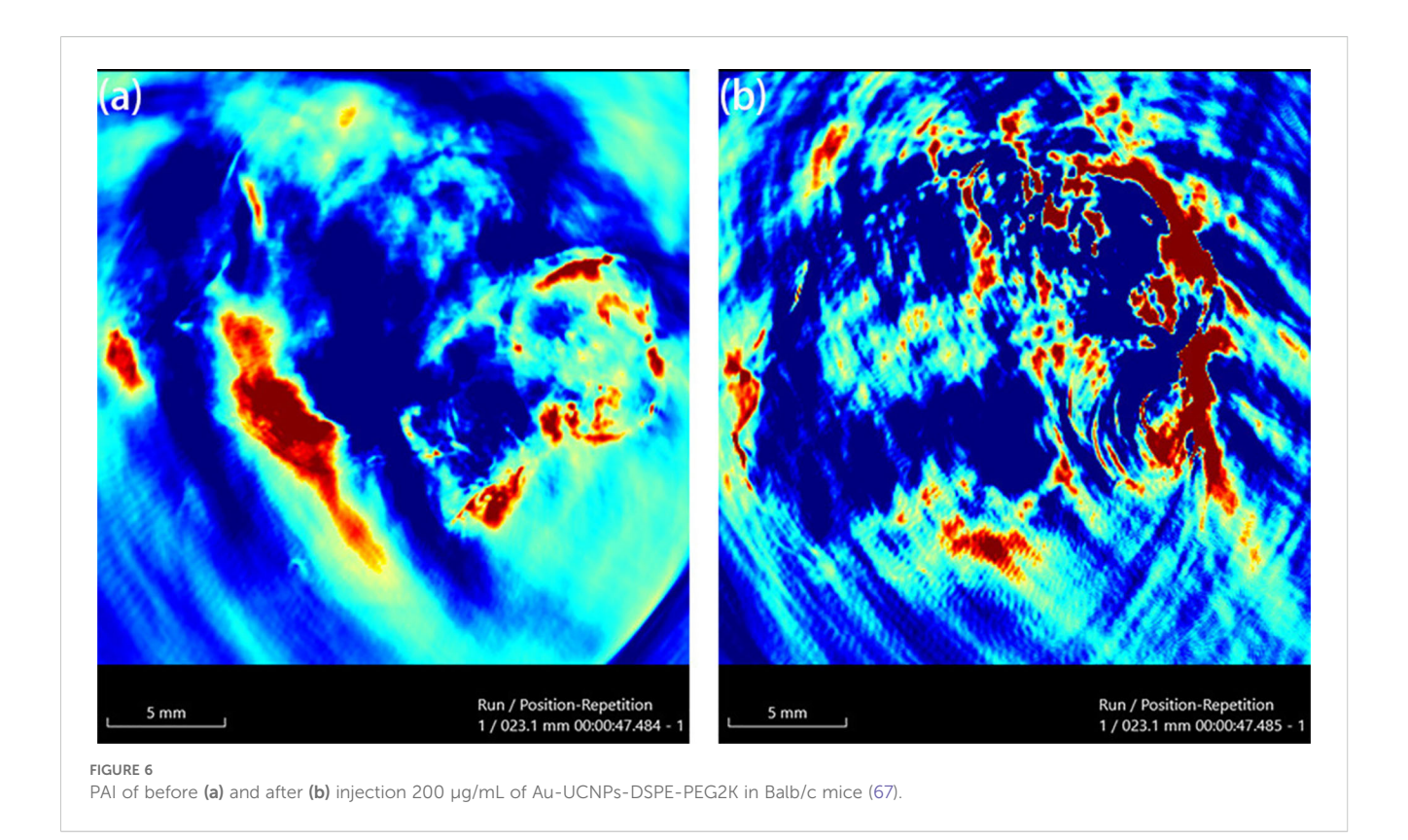
Beyond ligand-mediated targeting, tumor microenvironment (TME) characterized by hypoxia, low pH, elevated GSH, and ROS,

directs AuNPs accumulation. A TME-responsive platform bypasses ligand functionalization, exemplified by GSH-cleavable disulfide-linked AuNPs (~11nm, Brust-Schiffrin, spherical) achieving 98.7% MTX encapsulation for cervical cancer (69). Similarly, DOX-conjugated AuNPs utilize pH-labile hydrazone bonds that hydrolyze selectively in acidic TME conditions, enabling clinically translatable targeted therapy (66, 73).

Toxicity and complexity concerns around chemical stabilizers (e.g., 3MPA/3MPS/PVP) drove Kamini et al. to develop a novel PTX delivery platform (70). Their method synthesizes PTX-AuNPs in one step by adding silver ions to PTX/gold ion suspensions under sunlight (Figure 7), where PTX acts as both therapeutic payload and reducing/stabilizing agent (70). This eliminates pre-synthesized AuNPs and exogenous stabilizers, reducing costs while bypassing conventional drug-loading, though the photochemical mechanism requires further study (70).

2.2.2 Intrinsic antitumor effects of AuNPs

AuNPs exert intrinsic cytotoxicity against cervical cancer cells via apoptosis modulation (72, 74). Concentration-dependent upregulation of pro-apoptotic markers (BAX, p53) and downregulation of antiapoptotic factors (Bid, BCL-2) occur with concomitant caspase activation (75). This cascade initiates from AuNPs-induced intracellular ROS elevation, confirmed by flow cytometry showing increased cytoplasmic ROS and mitochondrial superoxide production (76). AuNPs generate ROS partly through intrinsic catalytic activity, converting H₂O₂ into H₂O and O₂ while enhancing catalase activity to modify the tumor microenvironment via hypoxia alleviation and immune potentiation (77). Additionally, AuNPs elevate superoxide dismutase (SOD) activity, causing H2O2 accumulation that activates caspase-dependent signaling pathways to induce cancer cell apoptosis (77). AuNPs' cytotoxicity against cervical cancer cells depends critically on nanoparticle diameter and subcellular localization (78). Dae et al. found extracellular monodisperse AuNPs prolong HeLa cell mitosis



without inducing apoptosis by forming division-disrupting nanobarriers. By contrast, 111nm extracellular AuNPs trigger ROS-mediated cell death with cytokinesis arrest, while 83nm particles cause transient M-phase delay followed by normal cytokinesis and G_1 -phase entry (78).

2.2.3 High-efficiency photothermal tumor ablation utilizing AuNPs

AuNPs act as efficient photothermal transducers, enabling precise tumor ablation under targeted guidance (21). Recent refinements include S-nitrosothiol-modified AuNPs releasing nitric oxide during PTT to simultaneously soften tumor extracellular matrix and generate mitochondrial reactive nitrogen species for enhanced cytotoxicity (79). Multibranched gold nanocrystals further outperform spherical or rod-shaped counterparts in photothermal conversion efficiency, confirming morphology as critical design parameter (21). PDT employs photosensitizers to generate cytotoxic ROS but faces limitations including toxicity and poor cellular uptake. Armin and team further demonstrated that AuNPs functionalized with protoporphyrin IX and FA via mercaptohexanol linkers enhance both cancer selectivity and cytotoxic efficiency (80).

2.2.4 Radiosensitization effects of AuNPs in radiotherapy

AuNPs enhance cervical cancer radiotherapy efficacy through their high atomic number (Z = 79), which dramatically exceeds biological elements. This promotes X-ray/ γ -ray absorption, generating amplified secondary electron fluxes that directly damage

tumor DNA (81). Radiation-activated gold nanorods (AuNPs, 54.6 ± 7.11 nm, spherical) further catalyze water decomposition, producing cytotoxic ROS (82). Functionalized variants concentrate radiation energy within lesions. Radiosensitization varies significantly with geometry: AuNRs surpass spheres (83). Nanocubes deposit 18.5% (18 MV) to 23.1% (6 MV) higher electron doses than nanospheres within 1.1 μ m radii, achieving maximum dose enhancement at 6 MV (84).

3 AuNPs in ovarian cancer

3.1 Diagnosis

3.1.1 Colorimetric detection utilizing AuNPs

Colorimetry enables rapid ovarian cancer biomarker screening but suffers from limited resolution. Eda et al. circumvented this via smartphone-integrated analysis leveraging mobile imaging hardware advances (~40nm) (85). Alternatively, Hao et al. engineered Mg/Felayered double hydroxide nanoflowers as high-density AuNPs (~10nm, Rapid injection synthesis) carriers for lateral flow immunoassay (LFIA) (86). These porous templates achieve ultrahigh AuNPs loading, lowering HE4 detection to 50 pM (86).

3.1.2 AuNPs-engineered electrochemical biosensors

CA125 is the clinical gold standard for ovarian cancer serology. Current AuNP-based detection platforms vary primarily in electrode composition and surface modification strategies(Table 5), integrating

 IABLE 4
 Design of AuNPs for the treatment of cervical cancer (drug delivery).

o Z	Particle size	Surface Particle size functionalization of AuNPs	Drug	Highlights of Study	Cell line	Toxic	Reference
	~11nm	Thiolation	MTX	AuNPs with FA modification; High MTX loading (>98.7% EE); GSH-responsive MTX release	U-87MG; HeLa; A549; PC3; HEK-293	The MTT results indicate no toxicity.	(69)
2	50.3 ± 1.1nm	Thiolation; Covalent bonding	DOX	Citraconic anhydride linker enables pH-responsive DOX release in tumor microenvironment	HeLa	Considered	(99)
8	~20nm	Thiolation	PTX	One-pot synthesis using PTX as dual reductant/stabilizer; Ecofriendly process without additional chemicals	SiHa; HT-29	Considered	(70)
4	18.30~21.16nm	Thiolation	Imiquimod	ASI411-mediated selective drug delivery; Enhanced vaginal tissue retention for gynecological cancer therapy	HeLa; HEC-1-A; NHDF; Franz	No toxicity	(72)
5	26.35 ± 2.13nm	Thiolation; Covalent bonding	DOX	pH-responsive DOX release; Dose-dependent cytotoxicity in HeLa cells, Synergistic therapeutic platform for ovarian cancer	HeLa	A dose-dependent toxicity was observed.	(73)

AuNPs with carbon nanomaterials (graphene, CNTs), polymers (chitosan, polydopamine, PAMAM), or novel frameworks (MXenes, MOFs) to enhance nanoparticle density, antigen capture efficiency, and electron transfer kinetics. The integration of MOFs with AuNPs achieves reproducible CA12-specific recognition, demonstrating a RSD of 2.98% in repeatability experiments (87). Zahra's MXene/GQD/AuNPs composite achieves a record LOD of 0.075nU/mL (88). DLS sensors offer the broadest linear range (5fg/ mL~50ng/mL) for high-dynamic CA125 quantification (89), while AuNP-DNA fluorescence quenching enables continuous biomarker monitoring. Near-field communication (NFC) integration further streamlines data acquisition, enhancing clinical utility (90).

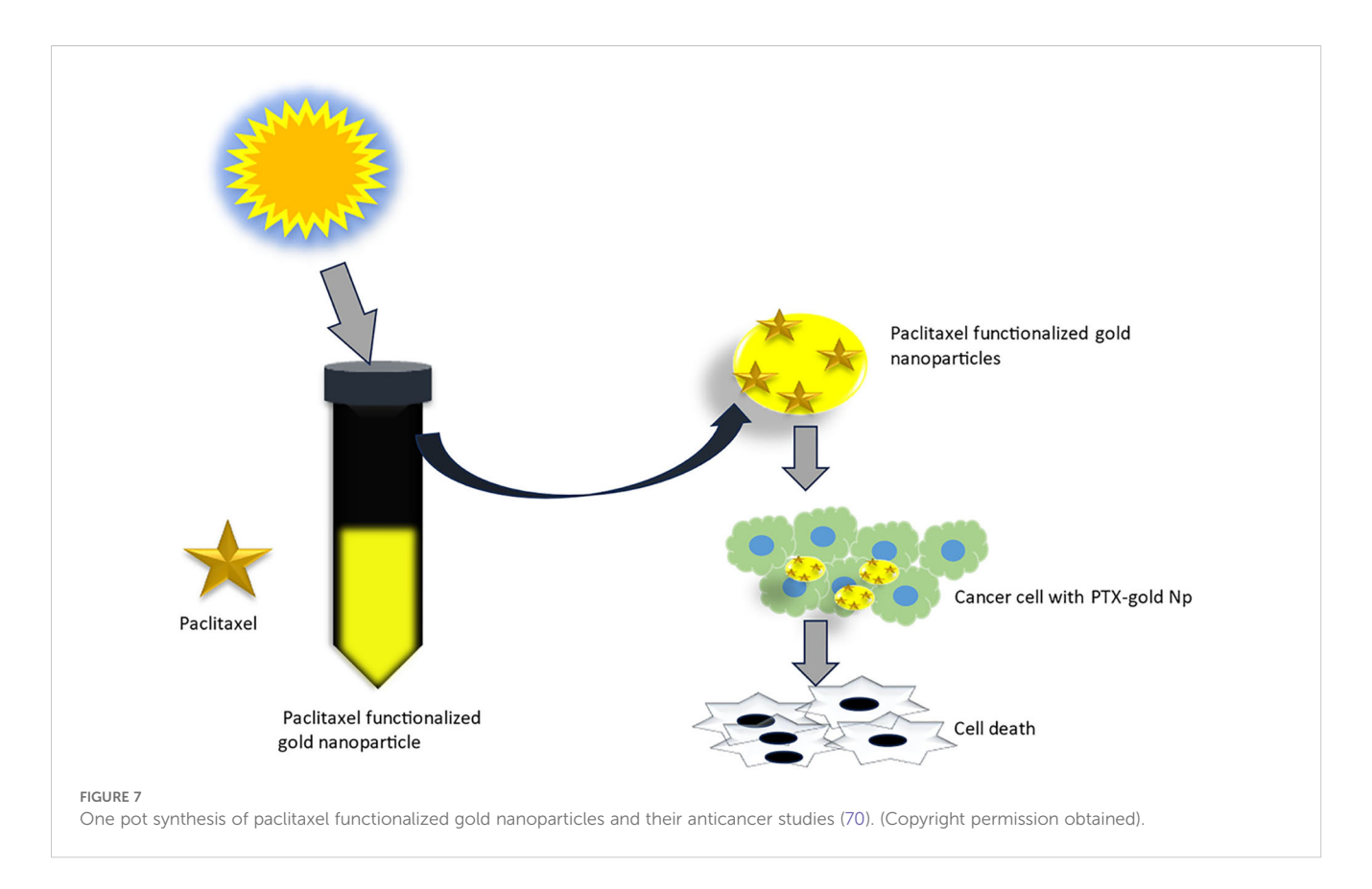
Beyond CA125, AuNP-based sensors target biomarkers including p53, HE4, exosomes, and DNA methylation (91, 103-106). Following Weiwei et al.'s MOF-AuNPs for CA125 (95), Xu and team developed a sandwich electrochemical immunosensor using synergistic signal amplification between Prussian blue (PB) and thiolated ionic MOF composites (TIMO+F-KB@AuNPs) for HE4 quantification (107). The platform employs TIMO+F-KB@AuNPs as conductive sensing substrates for capture antibody (Ab₁) immobilization, while PB nanoparticles carry detection antibodies (Ab₂). HE4 binding forms an Ab₁-HE4-Ab₂-PB complex, generating electrochemical signals proportional to concentration (linear range: 0.1~80ng/mL, LOD: 0.02ng/mL) (107). Demonstrating high selectivity, reproducibility, and stability with 97.10~114.07% serum recovery, it enables early ovarian cancer diagnosis (Figure 8). Separately, superparamagnetic CoFeB enhances AuNPs-based p53 detection (LOD: 0.006 U/mL) (104). Furthermore, exosomes predict ovarian cancer chemotherapy response. Meshach and team developed a cysteine-functionalized AuNP (Au-cys) biosensor using SERS to simultaneously capture cisplatin and small extracellular vesicles from biological samples, enabling concurrent early detection and treatment efficacy assessment (102).

AuNPs facilitate ovarian cancer diagnosis via urine, exhaled gas, and cyst fluid analysis (108, 109). Thomas and team pioneered nanopore sensing where AuNPs capture 13 cysteine-containing urinary peptides within α -hemolysin nanopores, generating distinct current signatures: stepwise reductions for small peptides versus polymorphic fluctuations for larger ones, enabling prolonged single-molecule characterization (108). AuNPs-based platforms also detect microbiome-derived Volatile organic compounds (VOCs) in exhaled breath with 82% screening accuracy (110).

3.1.3 AuNPs-enabled innovative imaging strategies

AuNPs drive transformative ovarian cancer imaging advances (19). Dheeraj and team engineered FA-targeted, hydrazinonicotinamide-chelated AuNPs enabling efficient 99mTc radiolabeling for tumor-specific single-photon emission computed tomography (SPECT) contrast (111). Further functionalization yielded GO/SPIO/AuNP composite sheets integrating PTT, radiotherapy, and MRI within a unified theranostic platform (112).

MARS spectral photon-counting CT (SPCCT), though primarily preclinical, enables material-specific imaging via energy-dependent X-ray attenuation. Dhiraj et al. functionalized AuNPs with LHRH via



PEG tethers for ovarian cancer targeting (113). Intraperitoneal administration in murine models achieved selective accumulation in peritoneal tumors (0.46~2.12ng/mg, ICP-MS). While current SPCCT sensitivity limited absolute quantification, it mapped gold distribution patterns (113). Increased LHRH density (3000~15000molecules/particle) enhanced targeting while maintaining >60% metabolic activity at therapeutic concentrations (12~30 μ g/mL), establishing a novel theranostic strategy (113).

Functionalized AuNPs support ovarian cancer-specific detection via fluorescence lifetime imaging (114), dark-field (115), and confocal Raman microscopy (116). SERS imaging further enables chemoresistance prediction and survival outcome assessment (117).

3.2 Treatment

3.2 .1. AuNPs-based drug delivery systems

AuNPs enable targeted ovarian cancer drug delivery, enhancing dispersion or internalization of agents like linalool, cetuximab, paclitaxel, let-7a miRNA, and nidocarcinoma-derived factor(Table 6). DOX-AuNPs show superior tumor growth inhibition versus free doxorubicin while overcoming payload leakage limitations (118). Engineered for MICU1-targeting siRNA delivery, they achieve >85% silencing efficiency via lysosome evasion, addressing key shortcomings of conventional carriers (119).

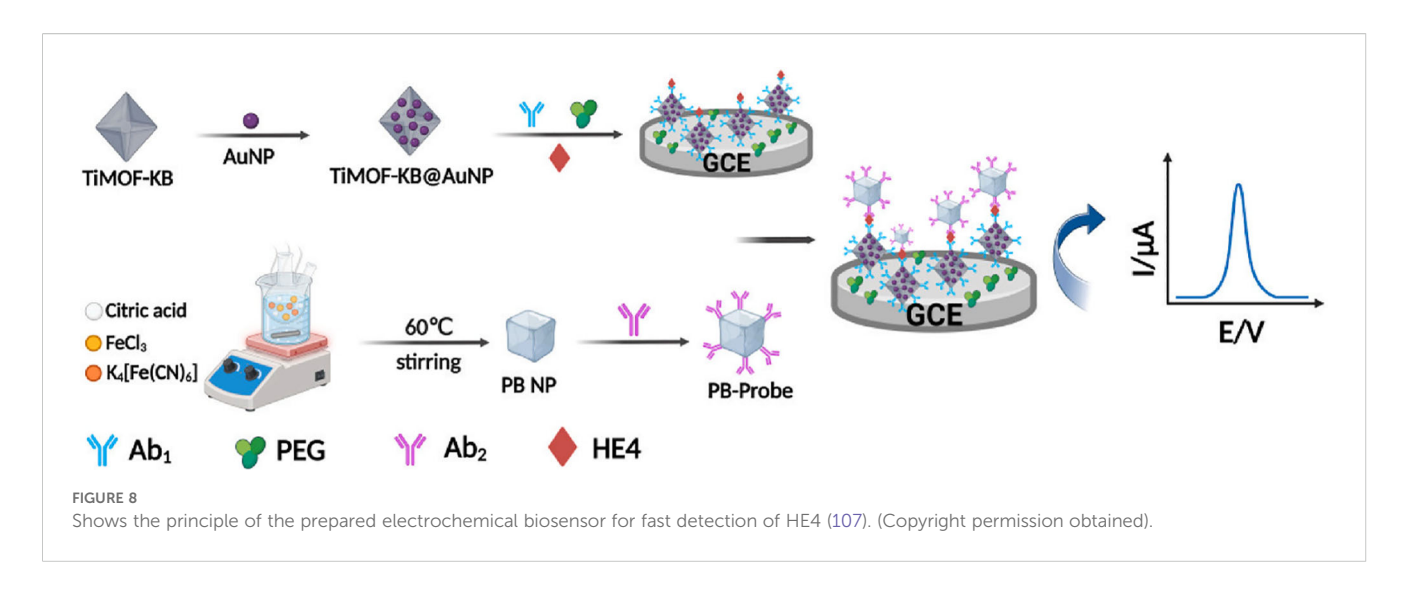
Antibody or peptide-conjugated AuNPs enable precise ovarian cancer targeting (128). Edison and team engineered FSH33-AuNPs

covalently conjugated to tumor-suppressive miR-145 (122). This system protects miR-145 from degradation, mediates selective cancer cell internalization, and inhibits proliferation, migration, anchorage-independent growth, and VEGF secretion. AuNPs enable co-delivery of multiple therapeutic agents, as demonstrated by Tommaso et al. who engineered miR-200c and trastuzumab (TZ)loaded nanoparticles that dual-target critical pathways driving SKOV3 cell survival and proliferation in vitro, overcoming TZ resistance while potentially improving therapeutic outcomes for HER2-positive ovarian cancer (126). Beyond antibody/peptide targeting, TME and hyperthermia trigger drug release from AuNPs,123. Reza et al. engineered antibody-conjugated magnetogold composites (TXT@Fe3O4/PVA/Au-SORT) for ovarian cancer (28). Photothermal AuNPs heating dissociates the PVA matrix, achieving precise TXT release (94.4 \pm 4.1% over 180 min in TME). Ca(OH)₂ pretreatment combined with TXT therapy enhanced intratumoral accumulation, inhibited migration, and induced DNA damage, achieving 78.3% tumor suppression with reduced systemic toxicity (Figure 9).

Notably, AuNPs morphology critically influences therapeutic outcomes: anisotropic AuNPs@CSA-131 exhibit enhanced cytotoxicity against ovarian carcinoma versus spherical counterparts (124). Furthermore, AuNPs modulate drug presentation *in vivo*, facilitating theaflavin oxidation to cytotoxic quinone derivatives (125). Regarding therapeutic side effects, The triple-modality approach (ultrasound/AuNCs/cisplatin) overcomes cisplatin resistance in resistant ovarian cancer models, suggesting reduced chemotherapy side effects with translational potential (129).

TABLE 5 Sensor design scheme for detecting CA125 based on AuNPs.

No	Particle size	Surface functionalization of AuNPs	Highlights of Study	Clinical sample	LOD	Linear range	Reference
1	-	-	Cu single-atom/AuNPs modified electrode	Artificial serum	0.37 pg/mL;1.58 pg/mL	0.005~500 ng/mL	(91)
2	~14nm	Thiolation; Covalent bonding	PAMAM/AuNPs and 3D rGO-MWCNTs modified electrode;Succinic anhydride-modified chitosan	Artificial serum	6 μU/mL	0.0005~75 U/mL	(92)
3	~15nm	Thiolation	$\label{eq:in-situ} \emph{In-situ} \ grown \ AuNPs/GaN \ Schottky junction \ via \ H_2O_2 \\ etching: AuNPs \ size-controlled \ Fermi \ level/charge \ transfer \\ efficiency$	Serum(4)	0.3 U/ml	1~100 U/mL	(93)
4	~13nm	-	Target-aptamer binding modulated AuNPs aggregation for fluorescence on/off;	Serum(4)	0.015 U/mL;7.5 pg/mL	0.01~2.0 U/mL;0.01~0.9 ng/mL	(94)
5	~13nm	Thiolation	Dual-signal detection: DLS particle size and fluorescence;	Serum(2)	1.1 fg/mL	5 fg/mL~50 ng/mL	(89)
6	-	Thiolation; Covalent bonding	Microporous carbon modified SPCE;Smartphone-based NFC signal acquisition;	Serum(6)	0.4 U/mL	0.5~50.0 U/mL	(90)
7	~4.5nm	-	TDN-enhanced TMSD with AuNPs/Ru/ZIF-MOF signal probes;	Serum(4)	0.006 pg/mL	0.01 pg/mL~10 ng/mL	(95)
8	122 ± 11nm	Thiolation	AuNPs modified FTO electrode;Oligonucleotide recognition elements (antibody-free);	Serum(3)	2.6 U/mL	10~800 U/mL	(96)
9	-	-	MXene-GQD/AuNPs modified electrode	Artificial serum	0.075 nU/mL	0.1 μU/mL~1 U/mL	(88)
10	-	Thiolation; Covalent bonding	AuNPs/RGO/PTH-modified DSPCE electrode	Artificial serum	0.069 pg/mL; 0.058 pg/mL	1~100 pg/mL	(97)
11	~70nm	-	AuNPs and DES-synthesized PTB co-modified SPCE	Artificial serum	1.20 pg/mL	5~100 pg/mL	(98)
12	-	-	Electrodes modified with MOF@AuNPs-based nanocomposites	Serum	7.185nU/mL	10~70nU/mL	(87)
13	-	Thiolation; Electrostatic adsorption	Two biocompatible 2D COFs (EP-TD-COF and AuNPs@COFBTT-DGMH) effectively preserved antibody activity and provided a favorable microenvironment, synergistically enhancing the stability and sensitivity of the immunosensor	Artificial serum	0.089mU/mL	0.00027~100U/mL	(99)
14	~54.61nm	-	The hybrid nanostructure of $\alpha\text{-MnO}_2$ nanorods and AuNPs enhanced conductivity and sensitivity	Serum	9.82ng/mL	10~70ng/mL	(100)
15	-	-	CuCo-ONSs@AuNPs nanocomposite-modified electrode	Serum(6)	39nU/mL	0.1μU/mL~1mU/mL	(101)
16	-	Thiolation	A biosensor capable of simultaneously interacting with sEV and CDDP was developed, enabling the simultaneous quantification of sEV and CDDP using SERS, thereby overcoming the heterogeneity and protein interference issues in SERS analysis of sEV	Positive serum(99); negative serum(20)	-	-	(102)



3.2.2 Intrinsic antitumor effects of AuNPs

AuNPs inhibit ovarian carcinoma invasiveness by targeting key oncogenic pathways: impeding MAPK signaling, suppressing EMT-associated proteins, and disrupting the IGFBP2/mTOR/ PTEN autoregulatory axis, downregulating IGFBP2, suppressing PI3K/AKT/mTOR activation, and reactivating PTEN (130, 131). Current understanding posits that AuNPs disrupt multicellular TME communication (cancer cells, cancer-associated fibroblasts, endothelial cells), downregulating pro-tumorigenic cytokines and growth factors (132, 133). Specifically, they reduce CC-secreted fibroblast-activating proteins (TGF-β1, PDGF, uPA, TSP1) and inhibit tumor angiogenesis by blocking VEGF-VEGFR2 signalling (133, 134). This positions AuNPs as key tools for elucidating and disrupting pro-tumorigenic crosstalk. AuNPs synchronize disulfidptosis and ferroptosis in ovarian cancer by modulating the SLC7A11/GSH/GPX4 axis (135). The composite system exploits AuNPs' glucose oxidase-like activity and Ap-mediated GLUT1 downregulation to induce metabolic crisis (135). Glucose deprivation limits NADPH replenishment, disrupting cystine/ cysteine conversion and resolving the disulfidptosis-ferroptosis execution paradox. Concurrently, iron-based components deliver Fe²⁺ while AuNPs-catalyzed glucose oxidation self-supplies H₂O₂, amplifying Fenton reactions and ferroptotic death (135).

Beyond influencing signalling pathways, AuNPs enhance nuclear rigidity via perinuclear laminA/C overexpression, impeding cancer cell migration (136). Concurrently, they induce ROS-mediated apoptosis/ autophagy, trapping cells in G0/G1 phase (137). Anisotropic AuNPs exert enhanced anti-migratory effects versus spherical counterparts (138). Analogous to cervical cancer applications, morphological engineering of AuNPs enhances their cytotoxic efficacy against ovarian cancer cells. Irfan et al. attribute this phenomenon to elongated-branched antibody-functionalized AuNPs effectively evading serum protein corona entrapment, thereby facilitating optimal aptamer binding to HER2 receptors on cancer cell surfaces (139). This mechanism induces significant cytotoxicity in HER2-overexpressing SKOV3 cells through targeted apoptosis initiation.

3.2.3 High-efficiency photothermal tumor ablation utilizing AuNPs

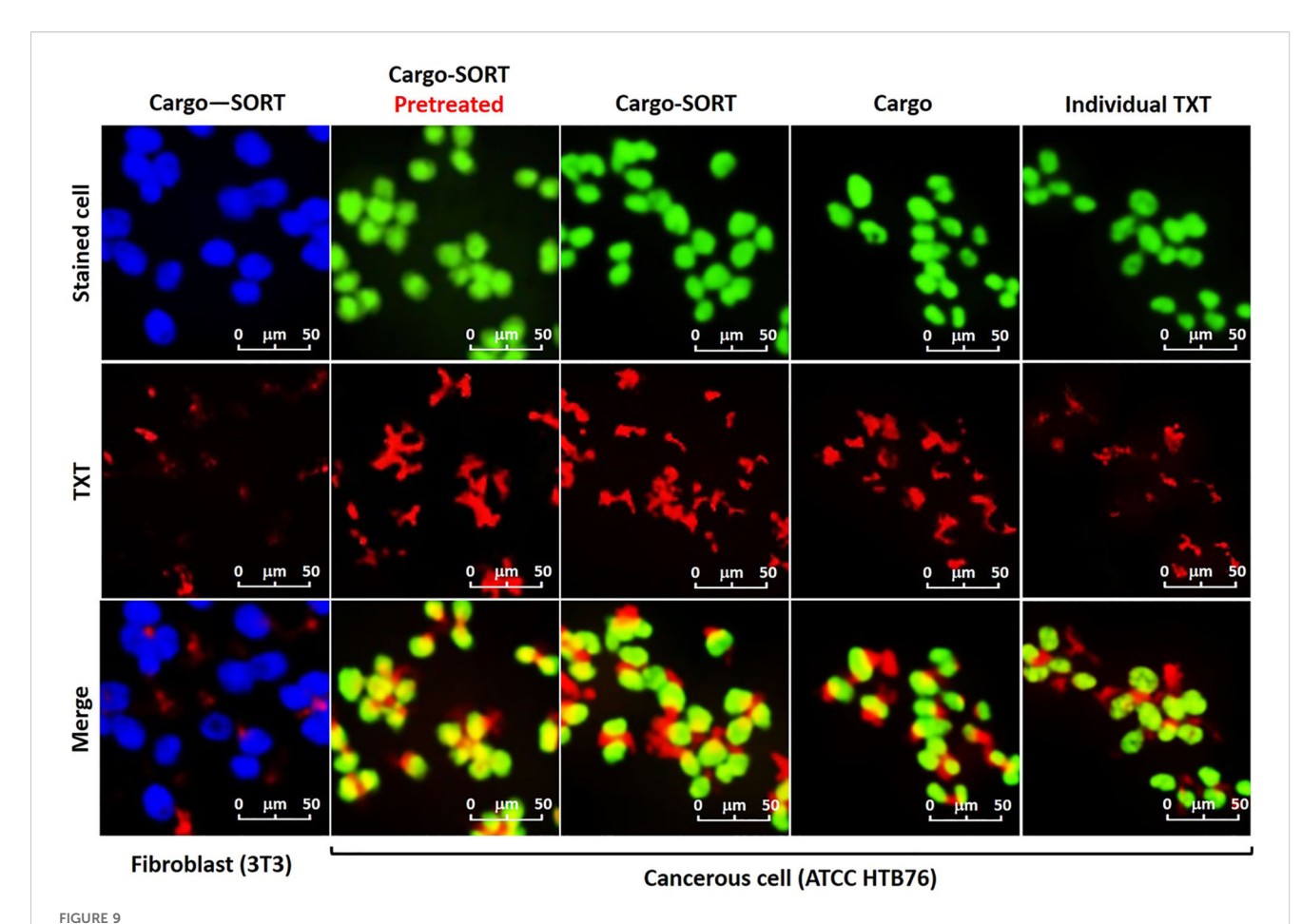
AuNPs enable synergistic chemo-photothermal therapy for ovarian cancer (127, 140). Yiting et al. engineered a genetically fused HSA nanocarrier (RHMH18@AuD) self-assembling via histidine hydrophobicity to encapsulate DTX while forming ultrasmall AuNPs through biomimetic mineralization (141). This 80-nm platform prevents HSA denaturation and reduces inorganic nanoparticle toxicity. MMP-2 cleavage at tumors releases RGD-HSA@Au (mediating photothermia) and His@DTX micelles, with acidic TME-triggered DTX release. The system demonstrated targeted cellular uptake, significant tumor suppression, and 100% survival at 70 days versus complete mortality in monotherapy groups by day 62, establishing a high-efficacy, low-toxicity therapeutic strategy.

Diverse AuNPs composites serve as photothermal agents for ovarian cancer PTT. rGO-AuNPs-PEG exhibits strong SERS signals, NIR-II PA signals, and high photothermal efficiency in tumours under 1061 nm laser irradiation (142). Similarly, silica nanocapsules containing aggregated AuNPs yolk-shell structures (aAuYS) demonstrate enhanced photothermal effects with 808 nm laser exposure (143). Curcumin-incorporated gold nanoshells (Cur-AuNShs) show efficient photothermal conversion with potential for selective cancer targeting and treatment. Additionally, AuNPs morphology influences PTT efficiency (144). For instance, dumbbell-shaped Au-Fe₃O₄ elevate thermal conversion efficacy (145).

To overcome resolution limitations in image-guided PTT, Annan et al. developed ultra-small GnRHR-targeted AuNDs (Au-GRHa, 3.2nm) (146). Prepared via electrochemical displacement and ligand conjugation, these nanoconstructs enable dual-modal fluorescence/CT imaging with superior CT contrast (attenuation coefficient: 5.153cm²/g) and renal clearance. GnRHa targeting boosted SKOV3 cellular uptake by 76% versus non-targeted counterparts. Under 808 nm irradiation, localized temperatures reached 50 °C within 5 min, inducing apoptosis via membrane disruption and protein denaturation. *In vivo* peak tumor

TABLE 6 Design of AuNPs for the treatment of ovarian cancer (drug delivery).

No	Particle size	Surface functionalization of AuNPs	Drug	Highlights of Study	Animal model	Toxic	Reference
1	~10nm	Covalent bonding	DTX	Plasmonic photothermal therapy (PPTT) enables pH-triggered controlled release of docetaxel by disrupting halloysite nanotube (HNT) interlayer hydrogen bonds via Au nanoparticle-mediated photothermal effects	-	The MTT results indicate low toxicity in 3T3	(115)
2	~13nm	Thiolation; Covalent bonding	CALNN;Linalool	GSH-capped linalool delivery; CALNN peptide conjugation; Caspase-8/p53 activation & NF-κB inhibition	-	Considered	(120)
3	~40nm	Thiolation	NDC - 1;NDC - 2	Thiol-Au conjugated naproxen derivatives; Simple high-loading platform; $5\times$ lower IC $_{50}$ vs free drugs	-	Considered	(121)
4	~13nm	Thiolation	DOX	DNA-hybridized Dox loading; pH-responsive release; 2.5× greater <i>in vivo</i> suppression vs free Dox	BALB/c nude mice	Considered	(118)
5	~20nm	-	auroliposome	AuNP-embedded siRNA liposomes; Caveolae-mediated uptake enhancement; PDX model efficacy	-	No toxicity	(119)
6	12 ± 2 nm	Thiolation	miR - 145	FSH receptor-targeted delivery via FSH33 peptide	-	Considered	(122)
7	~30nm	Electrostatic adsorption; Covalent bonding; Thiolation	PTX	Multimodal imaging (PA/FL/CT); pH-responsive PTX release; Photothermal-enhanced delivery	mice	Considered	(123)
8	~10nm	-	DTX	HNT/AuNP/SORT antibody integration; PPTT/pH-triggered release (44 °C activation); Selective cancer killing	-	The MTT results indicate low toxicity in 3T3	(115)
9	10~15nm	-	TXT	Ca(OH)2 tumor-penetration pretreatment; Magnetic/PPTT/CT multifunctional system; 89% growth inhibition	mice	The MTT results indicate low toxicity in 3T3	(28)
10	60 ± 5nm*30 ± 3nm	Thiolation; Covalent bonding	CSA-131	Peanut-shaped AuNP delivery of ceragenin; Systemic administration potential	BALB/c nude mice	No toxicity	(124)
11	~19nm	Thiolation; Covalent bonding	TfQ	Theaflavin-mediated synthesis/stabilization; Low hemolytic nanocomposite	-	No toxicity	(125)
12	~10nm	Thiolation	TZ; miR-200c	First integration of miR-200c with AuNPs-TZ nanocomplexes demonstrated.	-	Considered	(126)
13	~20nm	Thiolation	DOX	QbD-guided functionalization yielded pH/NIR-responsive AuNPs-L-Dox nanoplatform for selective tumor drug release with reduced systemic toxicity	-	Low toxicity	s(127)



Confocal images of the subjected TXT@Fe3O4/PVA/Au nano-therapeutic to the stained cells. Green: HTB76 cancerous, and blue: NIH 3T3 fibroblast cells (106 DFU), in the presence of the individual TXT, TXT@Fe3O4/PVA/Au (Cargo), and TXT@Fe3O4/PVA/Au-SORT particles (Cargo-SORT) particles. Cell staining was performed using crystal violet, and incubation was carried out at 37 °C with 95% humidity for 2 hours. Pretreatment was done with Ca(OH)2@Fe3O4/PVA/Au-SORT particles in the same dosage with the TXT-containing therapeutic ($10\mu g/mL$) (28).

accumulation occurred at 2 h, with subsequent PTT significantly suppressing tumor growth without hemolysis or toxicity, establishing a precise image-guided therapeutic platform.

PDT and PTT act synergistically against ovarian cancer. A multifunctional nanomicrogel (Au@MSN-Ter/THPP@CM@GelMA/CAT) demonstrates concurrent photodynamic efficacy (650nm) and photothermal ablation (980nm) (147).

3.2.4 Radiosensitization effects of AuNPs in radiotherapy

AuNPs exhibit radiosensitizing effects, exemplified by thioglucose-bound nanoparticles (Glu-GNPs) enhancing ovarian cancer radiotherapy (148). The GO-SPIO-Au nanoflower platform integrates graphene oxide (NIR-PTT), AuNPs (radiosensitization), and superparamagnetic iron oxide (MRI) for image-guided therapy (112). In murine models, combined PTT/RT yielded 1.85× and 1.44× higher efficacy than PTT or RT alone, respectively. Kinga et al. developed a novel cancer therapy combining antibody-drug conjugates (ADCs) with β -emitting ¹⁹⁸AuNPs conjugated to trastuzumab emtansine (T-DM1), demonstrating specific HER2 affinity and synergistic efficacy against HER2-overexpressing cancers at low T-DM1 doses (0.015~0.124µg/mL) with 10–20

MBq/mL radiation (149). Continuous 7-day treatment (20 MBq/mL+0.031µg/mL T-DM1) disrupted 3D tumor spheroids, suggesting potential for HER2-positive breast/ovarian cancer treatment despite preferential suitability of inorganic nanoradiopharmaceuticals for localized delivery (Figure 10) (149).

4 Integrated diagnostic and therapeutic platform

AuNPs serve as pivotal components in multimodal theranostic platforms owing to their distinctive physicochemical properties, enabling visualized precision therapy of pathological lesions. Diversified therapeutic strategies demonstrate that targeted accumulation of AuNPs at disease sites generates synergistic effects, with imaging guidance being critical for maximizing diagnostic-therapeutic efficacy. Current research has developed functionalized AuNPs-based visualization approaches for gynecological malignancies. Zhang's team overcame single-modality imaging limitations by establishing a PAI/CT/MRI multimodal system centered on functionalized AuNPs, effectively addressing the low X-ray attenuation coefficient inherent to

inorganic materials (67). At 200 µg/mL, Au-UCNPs-DSPE-PEG precisely delineated cervical cancer location, dimensions and morphological characteristics in murine models, while their photothermal conversion capability simultaneously enabled photoacoustic imaging-guided combination photothermal and photodynamic therapy (67). Beyond physical modalities, AuNPs function as chemotherapeutic carriers. Taheri et al. employed CT to monitor TXT@AuNPs distribution for efficacy assessment, yet single-modality CT proved inadequate for tracking drug release kinetics (28). Wang's team addressed this through multimodal imaging (PAI/FL/CT) for real-time surveillance of drug-loaded AuNPs. Paclitaxel release induced fluorescence signal fluctuations due to AuNP surface restructuring while accelerating nanoparticle metabolic clearance, consequently reducing photoacoustic intensity in lesions (123). For quantitative release monitoring, Yim's team innovatively leveraged AuNPs' low X-ray attenuation property (66). Electrostatic adsorption-triggered aggregation of radioiodinated AuNPs, occurring through opposite surface charges after DOX release, significantly enhanced lesion signals on PET-CT imaging (66). These aggregates maintained prolonged high-signal states due to extended half-life, enabling sustained dynamic observation.

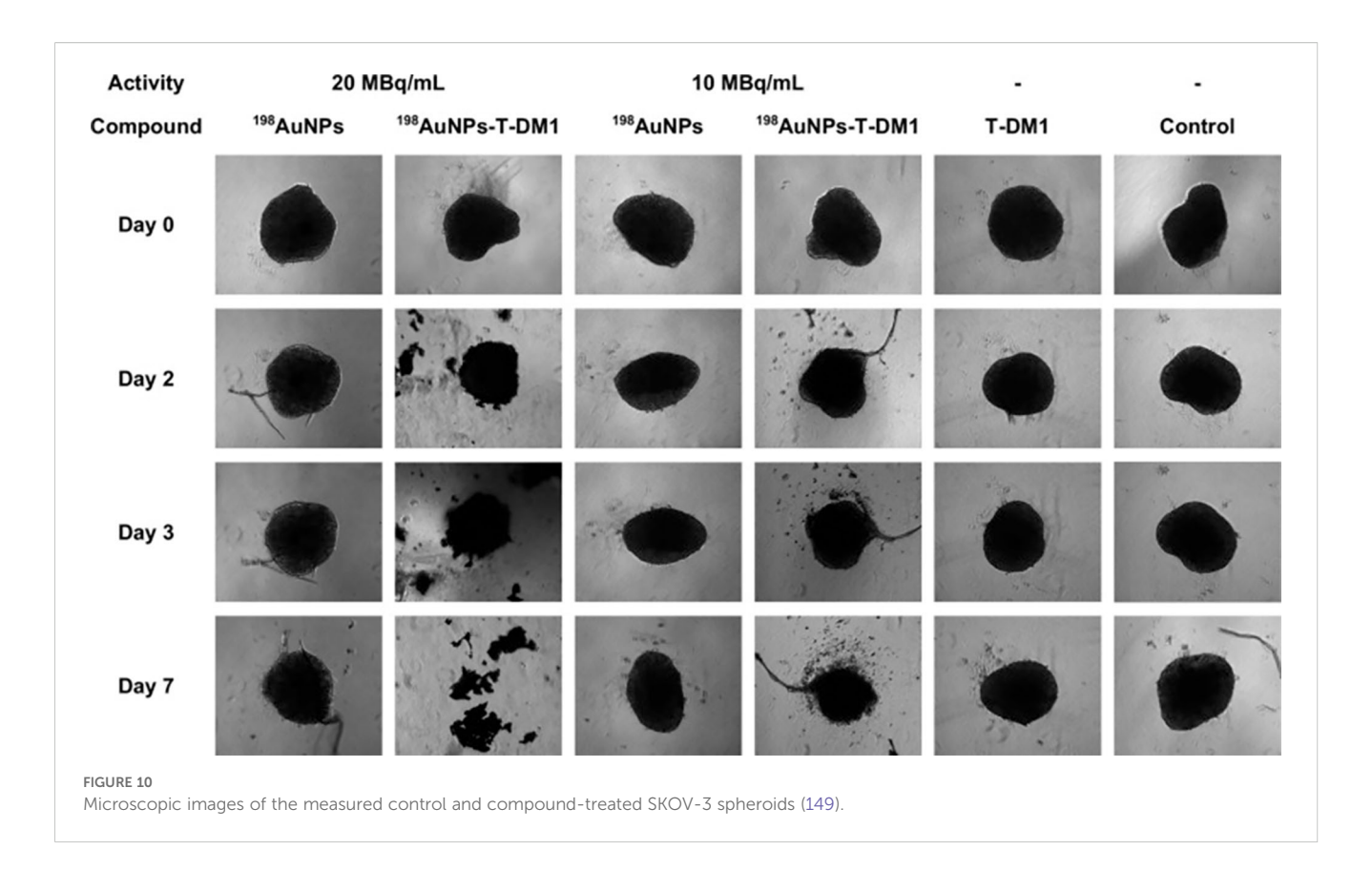
5 Challenges and limitations

Despite being a promising nanomaterial, AuNPs must overcome several significant barriers prior to broad clinical adoption for diagnosing and treating gynecological malignancies.

The safety profile of AuNPs represents a modifiable property, critically dependent on factors such as particle size, synthesis method, exposure route, dosage duration, and the specific biological milieu (150, 151). In numerous studies cited above, AuNPs are often assumed to be chemically inert and stable materials, particularly when PEG-modified, exhibiting negligible toxicity at certain doses. Merely 28 investigations to date have employed MTT assays and related techniques to evaluate the cytotoxicity of novel functionalized AuNPs toward normal cells or animal models. In the clinical context of managing gynecological malignancies, chemotherapy is typically a protracted process (152). Repeated administration of functionalized AuNPs during such long-term treatment carries a significant risk of inducing antibodies against the nanoparticle surface characteristics. This immunogenic response could potentially compromise the targeting efficacy of AuNPs and disrupt normal immune function. Furthermore, diverse AuNPs synthesis and functionalization strategies can leave toxic chemical residues on the particle surfaces. These modifications also alter the chemical properties and size of the AuNPs, potentially hindering renal clearance and leading to progressive bioaccumulation. Additionally, compared to free drugs, administering chemotherapeutic nanoparticles during ovulation increases ovarian toxicity and reduces fertility (153). Therefore, the menstrual cycle warrants consideration in the design and implementation of AuNPs therapies for female patients. These concerns underscore the necessity for further comprehensive evaluation of AuNPs systemic safety in humans and detailed investigation into nanoparticle pharmacokinetics to fully assess their absorption, distribution, metabolism, and excretion processes.

Addressing AuNP safety challenges requires systematic pharmacokinetic studies (absorption, distribution, metabolism, excretion) in animal models to define critical thresholds for nanoparticle-induced irreversible organ damage, enabling establishment of dimensionally-, morphologically-, and synthesismethod-dependent safety dosage windows across varied administration regimens. Green synthesis strategies utilizing novel catalysts demonstrate promising toxicological safety profiles, potentially representing key advancement pathways (75, 76). Multifunctional AuNPs may shorten chemotherapy cycles while combined PTT and PDT therapies could circumvent antibody responses from chronic treatment (127, 141). Nevertheless, large-scale animal validation remains indispensable; current maximum reported cohort sizes of 28 subjects prove insufficient, particularly given physiological disparities between rodent and human systems, necessitating expansion to rabbit and non-human primate models. These imperatives collectively emphasize comprehensive assessment of systemic AuNP safety in humans and rigorous pharmacokinetic investigation.

The diagnostic and therapeutic efficacy of AuNPs requires further validation. The majority of studies demonstrating potential benefits are confined to cell lines or small animal models, overlooking the substantial complexity of human physiology. In cervical cancer diagnostics, merely 15 of 34 peerreviewed investigations disclosed clinical sample accuracy (n=9) or spiked serum analyte recovery (n=6), with two HPV detection reports achieving >95% accuracy in cohorts exceeding 100 specimens. Regarding therapeutic applications, only 2 of 15 cervical cancer publications documented AuNP efficacy in murine models. Similarly, among 28 ovarian cancer diagnostic analyses, 18 provided clinical validation data (n=4) or serum recovery metrics (n=14), though clinical specimens numbered ≤10 per analysis. Whereas 21 of 28 therapeutic investigations asserted significant antitumor outcomes, merely 9 confirmed efficacy in animal models with quantification parameters undisclosed. Humans are continuously exposed throughout life to diverse natural and anthropogenic nanoparticles. Such environmental nanoparticle contamination constitutes a significant exogenous interference factor, potentially impeding the function of administered AuNPs. For instance, titanium or iron oxide nanoparticles can inhibit cancer cell uptake of AuNPs (154). Beyond these exogenous factors, endogenous human variables also critically influence AuNPs performance. Evidence indicates that elevated cholesterol levels and specific lipid ratios disrupt the delivery capacity of DOX-AuNPs systems (155). Even in Phase III clinical trials, AuNPs-based drug delivery systems demonstrated suboptimal recognition efficiency for ovarian cancer, with the majority of intratumoral nanoparticles becoming either trapped within the extracellular matrix or sequestered by perivascular tumor-associated

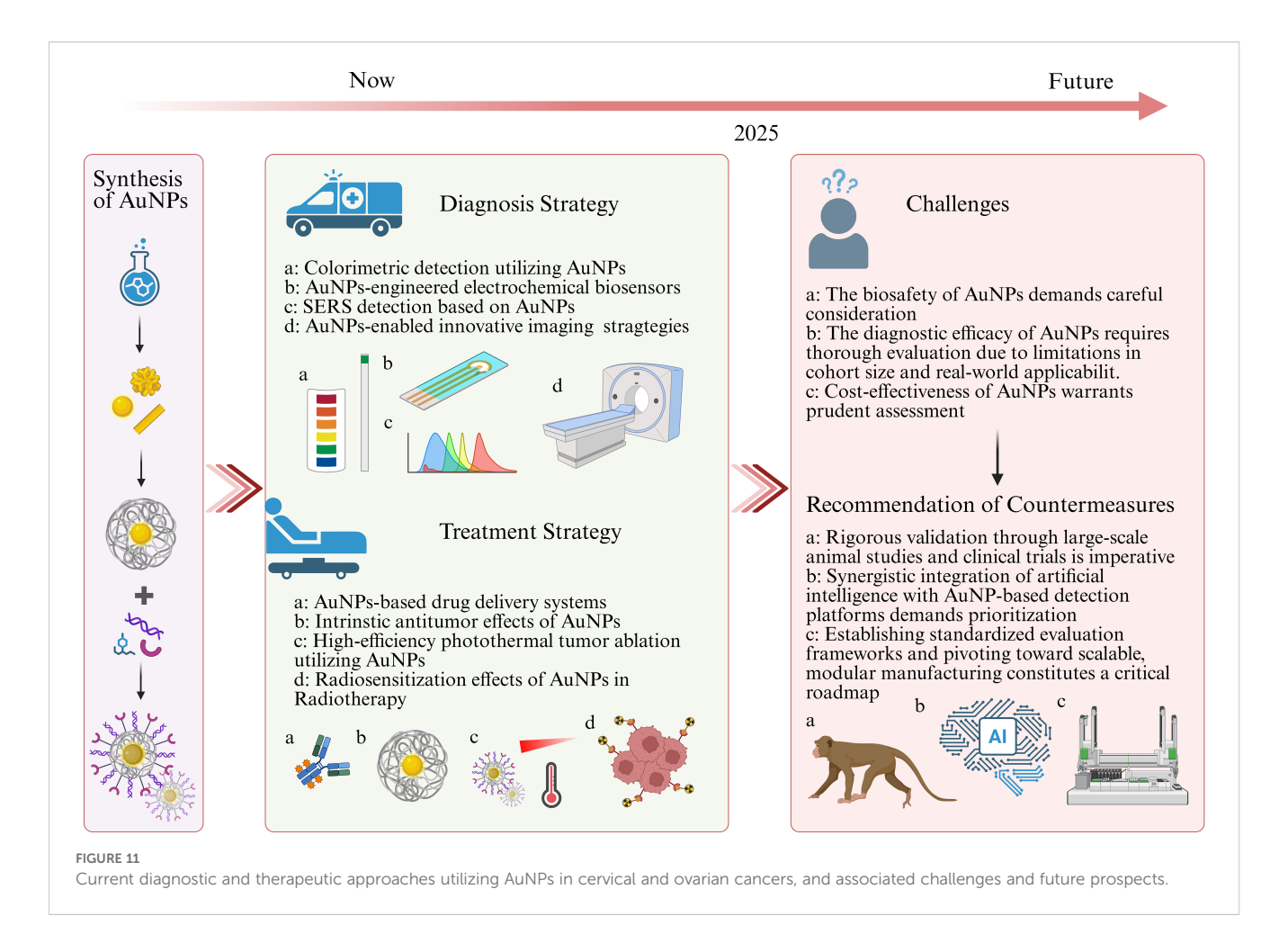


macrophages (156). Compounding these issues, many studies report human validation based on single-digit sample cohorts, lacking comparison with healthy individuals or non-gynecological cancer patients, and frequently omit detailed accuracy data (Supplementary Material 1).

Subsequent investigations must validate AuNPs' true diagnostic-therapeutic efficacy through large-scale animal models and clinical trials, with priority assessment of their resistance to complex biological interferences including protein corona formation and lipid adsorption. Although functionalized AuNPs demonstrate anti-interference capabilities in select studies, the disparity between simulated laboratory conditions and physiological environments necessitates rigorous in vivo verification. Novel non-spherical geometries such as high-aspectratio nanostars effectively circumvent protein corona shielding while enhancing tumor targeting precision (139). Notably, nanoparticles within the 10~20 nm size range exhibit optimal performance, yet synthesis-dependent variations in AuNP dimensions/morphologies demand standardized evaluation frameworks to enable cross-study comparability and collaborative advancement. Furthermore, addressing prevalent data limitations stemming from insufficient clinical samples requires establishing multicenter validation frameworks. AuNPs' therapeutic potential should transcend conventional drug delivery roles toward multimodal theranostic platforms, exemplified by triple-modality regimens integrating PTT, controlled chemotherapeutic release, and radiosensitization, with concurrent treatment monitoring via PAI and PET-CT. While four diagnostic investigations have incorporated machine learning for enhanced SERS-based highthroughput chip detection, deep learning applications in medical image interpretation remain unexplored. Integrating big data analytics with mobile health technologies could establish intelligent diagnostic networks to reduce misinterpretation risks.

Finally, the cost implications of AuNPs systems demand serious consideration. In resource-limited developing nations, economic constraints remain pivotal in restricting large-scale disease screening initiatives. Most current studies fail to address the cost structure of AuNPs-based diagnostic platforms, with only a handful reporting screening expenses or reusability metrics (157). A predominant focus on novel materials and intricate architectures, particularly acute within the domain of AuNPs-designed electrochemical sensors, often overshadows the underlying premise of screening: low cost and high accessibility. Furthermore, AuNPs synthesis methodologies themselves represent significant cost determinants, compounded by concerns regarding environmental impact and suboptimal production efficiency (151). These factors establish cost as a paramount consideration for the clinical translation of AuNPs technologies.

The convergence of artificial intelligence and low-cost smartphones offers a significant pathway to reduce expenditures associated with AuNP-based diagnostic systems, effectively lowering human resource requirements, time costs, and sample transport losses. Implementing a three-tier diagnostic network comprising colorimetric detection units, subject mobile client devices, and hospital data centres substantially enhances population screening efficiency. A core advantage of this system lies in the capacity for AI algorithms to perform localized processing directly on smartphones, enabling preliminary



screening and interpretation of test results; only data indicating anomalies require transmission to the hospital data centre for verification, thereby markedly alleviating the healthcare burden in resource-limited settings. This tiered network fundamentally transforms the traditional hierarchical "hospital-centrichealthcare worker-subject" information delivery model. By empowering subjects with autonomous testing capabilities, it shifts the paradigm from passive information reception to proactive health management, significantly improving participant engagement and adherence. From a technological development perspective, research efforts should recalibrate their focus regarding AuNPs: prioritizing material design optimization that establishes an optimal cost-accuracy balance over the pursuit of increasingly complex material combinations; directing energy towards developing scalable, low-power manufacturing processes; and advancing clinical integration through modular designs that reduce the overall system cost.

Notably, clinical trials of AuNPs in gynaecological malignancies remain limited. However, recent human studies across non-gynaecological cancers, spanning breast cancer, colorectal carcinoma and cutaneous disorders, demonstrate expanding clinical evaluation (158–162). These advances confirm that current implementation challenges are addressable and reveal

diagnostic and therapeutic benefits warranting further translation in gynaecological oncology. Collectively, AuNPs systems exhibit significant potential for enhancing diagnostic accuracy, improving patient quality of life, and optimizing clinical prognoses. Looking forward, their unique physicochemical properties position AuNPs as transformative agents in next-generation gynecologic oncology, enabling minimally invasive theranostics, real-time disease monitoring, and personalized treatment regimens. Continued advancements in nanomaterial engineering, refined targeting methodologies, comprehensive safety evaluations, and integration of AI further solidify AuNPs platforms to assume an increasingly critical and expansive role in future integrated theranostic frameworks (Figure 11).

6 Conclusion

Clinical management of gynecological malignancies faces significant challenges, including difficulties in early detection, high therapeutic resistance, substantial risks of residual disease post-surgery, and considerable toxicity from conventional radiotherapy and chemotherapy. These critical limitations demand innovative technological solutions for precision diagnostics and therapeutics.

Recent advances in nanotechnology provide transformative momentum for gynecologic oncology, with AuNPs offering particularly promising strategies due to their tunable dimensions, morphological versatility, customizable surface functionalization, and unique optical properties. AuNPs serve as highly sensitive contrast agents that enhance detection rates for early-stage lesions and micrometastases. Functionalization with antibodies, peptides, or aptamers enables precise targeting of therapeutic payloads to disease sites and facilitates ultrasensitive detection of trace biomarkers in liquid biopsies. Furthermore, their exceptional photothermal conversion efficiency and photochemical capabilities permit concurrent targeted chemotherapy with spatially precise photothermal and photodynamic therapy at tumor sites. This integrated theranostic approach positions AuNPs-based systems to drive a paradigm shift from isolated interventions toward closed-loop precision management in gynecologic oncology. Nevertheless, further validation remains imperative to address clinical translation barriers and long-term safety profiles.

Author contributions

SZ: Data curation, Formal Analysis, Methodology, Software, Writing – original draft. TL: Data curation, Writing – original draft. DJ: Data curation, Formal Analysis, Methodology, Writing – original draft. HS: Data curation, Formal Analysis, Writing – review & editing. HH: Supervision, Writing – review & editing. ZF: Funding acquisition, Resources, Writing – review & editing. XS: Writing – review & editing.

Funding

The author(s) declare financial support was received for the research and/or publication of this article. This study was financially supported by the National Natural Science Foundation of China (NO.82173327, NO.82272916).

References

- 1. Mahmoodi P, Fani M, Rezayi M, Avan A, Pasdar Z, Karimi E. Early detection of cervical cancer based on high-risk HPV DNA-based genosensors: A systematic review. *Biofactors.* (2019) 45:101–17. doi: 10.1002/biof.1465
- 2. Zarocostas J. Renewed calls to scale-up cervical cancer screening. Lancet. (2024) 403:797. doi: 10.1016/S0140-6736(24)00408-2
- 3. Lycke KD, Kahlert J, Petersen LK, Damgaard RK, Cheung LC, Gravitt PE. Untreated cervical intraepithelial neoplasia grade 2 and subsequent risk of cervical cancer: population based cohort study. *BMJ.* (2023) 383:e075925. doi: 10.1136/bmj-2023-075925
- 4. Cremer M, Alfaro K, Masch R. Cervical cancer screening in low- and middle-income countries. JAMA. (2021) 325:790. doi: 10.1001/jama.2020.25214
- 5. Menon U, Gentry-Maharaj A, Burnell M, Singh N, Ryan A, Karpinskyj C. Ovarian cancer population screening and mortality after long-term follow-up in the UK Collaborative Trial of Ovarian Cancer Screening (UKCTOCS): a randomised controlled trial. *Lancet.* (2021) 397:2182–93. doi: 10.1016/S0140-6736(21)00731-5
- 6. Armstrong DK, Alvarez RD, Backes FJ, Bakkum-Gamez JN, Barroilhet L, Behbakht K. NCCN guidelines[®] Insights: ovarian cancer, version 3.2022. *J Natl Compr Canc Netw.* (2022) 20:972–80. doi: 10.6004/jnccn.2022.0047

Acknowledgments

We also thank Biorender for the templates used in the graphical abstract and Figure 11.

Conflict of interest

The authors declare that the research was conducted in the absence of any commercial or financial relationships that could be construed as a potential conflict of interest.

Generative AI statement

The author(s) declare that no Generative AI was used in the creation of this manuscript.

Any alternative text (alt text) provided alongside figures in this article has been generated by Frontiers with the support of artificial intelligence and reasonable efforts have been made to ensure accuracy, including review by the authors wherever possible. If you identify any issues, please contact us.

Publisher's note

All claims expressed in this article are solely those of the authors and do not necessarily represent those of their affiliated organizations, or those of the publisher, the editors and the reviewers. Any product that may be evaluated in this article, or claim that may be made by its manufacturer, is not guaranteed or endorsed by the publisher.

Supplementary material

The Supplementary Material for this article can be found online at: https://www.frontiersin.org/articles/10.3389/fonc.2025.1664340/full#supplementary-material

- 7. Konstantinopoulos PA, Matulonis UA. Clinical and translational advances in ovarian cancer therapy. *Nat Cancer*. (2023) 4:1239–57. doi: 10.1038/s43018-023-00617-9
- 8. Xu M, Cao C, Wu P, Huang X, Ma D. Advances in cervical cancer: current insights and future directions. *Cancer Commun (Lond)*. (2025) 45:77–109. doi: 10.1002/cac2.12629
- 9. Dai W, Zhou J, Chen T. Unraveling the extracellular vesicle network: insights into ovarian cancer metastasis and chemoresistance. *Mol Cancer*. (2024) 23:201. doi: 10.1186/s12943-024-02103-x
- 10. Zhou Y, Yuan J, Xu K, Li S, Liu Y. Nanotechnology reprogramming metabolism for enhanced tumor immunotherapy. *ACS Nano*. (2024) 18:1846–64. doi: 10.1021/acsnano.3c11260
- 11. Jokerst JV, Cole AJ, Van de Sompel D, Gambhir SS. Gold nanorods for ovarian cancer detection with photoacoustic imaging and resection guidance via Raman imaging in living mice. ACS Nano. (2012) 6:10366–77. doi: 10.1021/nn304347g
- 12. Hyun H, Sun B, Yazdimamaghani M, Wielgus A, Wang Y, Montgomery SA. Tumor-specific surface marker-independent targeting of tumors through nanotechnology and bioorthogonal glycochemistry. *J Clin Invest.* (2025) 135: e184964. doi: 10.1172/JCI184964

- 13. Maksymova L, Pilger YA, Nuhn L, Van Ginderachter JA. Nanobodies targeting the tumor microenvironment and their formulation as nanomedicines. *Mol Cancer*. (2025) 24:65. doi: 10.1186/s12943-025-02270-5
- 14. Li SR, Tao SY, Li Q, Hu CY, Sun ZJ. Harnessing nanomaterials for copper-induced cell death. *Biomaterials*. (2025) 313:122805. doi: 10.1016/j.biomaterials.2024.122805
- 15. Caputo D, Quagliarini E, Coppola A, La Vaccara V, Marmiroli B, Sartori B, et al. Inflammatory biomarkers and nanotechnology: new insights in pancreatic cancer early detection. *Int J Surg.* (2023) 109:2934–40. doi: 10.1097/JS9.00000000000000558
- 16. Nasrollahpour H, Khalilzadeh B, Hasanzadeh M, Rahbarghazi R, Estrela P, Naseri A. Nanotechnology-based electrochemical biosensors for monitoring breast cancer biomarkers. *Medicinal Res Rev.* (2023) 43:464–569. doi: 10.1002/med.21931
- 17. Medici S, Peana M, Coradduzza D, Zoroddu MA. Gold nanoparticles and cancer: Detection, diagnosis and therapy. *Semin Cancer Biol.* (2021) 76:27–37. doi: 10.1016/j.semcancer.2021.06.017
- 18. Dastgheib ZS, Abolmaali SS, Farahavar G, Salmanpour M, Tamaddon AM. Gold nanostructures in melanoma: Advances in treatment, diagnosis, and theranostic applications. *Heliyon*. (2024) 10:e35655. doi: 10.1016/j.heliyon.2024.e35655
- 19. Nanda BP, Rani P, Paul P, Aman, Ganti SS, Bhatia R. Recent trends and impact of localized surface plasmon resonance (LSPR) and surface-enhanced Raman spectroscopy (SERS) in modern analysis. *J Pharm Anal.* (2024) 14:100959. doi: 10.1016/j.jpha.2024.02.013
- 20. Xu T, Geng Z. Strategies to improve performances of LSPR biosensing: Structure, materials, and interface modification. *Biosens Bioelectron*. (2021) 174:112850. doi: 10.1016/j.bios.2020.112850
- 21. Zhu D, Liu Y, Liu M, Liu X, Prasad PN, Swihart MT. Galvanic replacement synthesis of multi-branched gold nanocrystals for photothermal cancer therapy. *J Mater Chem B*. (2020) 8:5491–9. doi: 10.1039/d0tb00748j
- 22. Mellor RD, Uchegbu IF. Ultrasmall-in-nano: why size matters. Nanomater (Basel). (2022) 12:2476. doi: 10.3390/nano12142476
- 23. Ward LC, Brantlov S. Bioimpedance basics and phase angle fundamentals. Rev Endocr Metab Disord. (2023) 24:381–91. doi: 10.1007/s11154-022-09780-3
- 24. Li Y, Tang L, Zhu C, Liu X, Wang X, Liu Y. Fluorescent and colorimetric assay for determination of Cu(II) and Hg(II) using AuNPs reduced and wrapped by carbon dots. *Mikrochim Acta*. (2021) 189:10. doi: 10.1007/s00604-021-05111-6
- 25. Zhang L, Mazouzi Y, Salmain M, Liedberg B, Boujday S. Antibody-gold nanoparticle bioconjugates for biosensors: synthesis, characterization and selected applications. *Biosens Bioelectron*. (2020) 165:112370. doi: 10.1016/j.bios.2020.112370
- 26. Yin T, Yang T, Chen L, Tian R, Cheng C, Weng L. Intelligent gold nanoparticles for Malignant tumor treatment via spontaneous copper manipulation and on-demand photothermal therapy based on copper induced click chemistry. *Acta Biomater*. (2023) 166:485–95. doi: 10.1016/j.actbio.2023.04.036
- 27. Cao J, Lv P, Shu Y, Wang J. Aptamer/AuNPs encoders endow precise identification and discrimination of lipoprotein subclasses. *Biosens Bioelectron*. (2022) 196:113743. doi: 10.1016/j.bios.2021.113743
- 28. Taheri-Ledari R, Zolfaghari E, Zarei-Shokat S, Kashtiaray A, Maleki A. A magnetic antibody-conjugated nano-system for selective delivery of Ca(OH)2 and taxotere in ovarian cancer cells. *Commun Biol.* (2022) 5:995. doi: 10.1038/s42003-022-03966-w
- 29. S R, M P. Multi-functional FITC-silica@gold nanoparticles conjugated with guar gum succinate, folic acid and doxorubicin for CT/fluorescence dual imaging and combined chemo/PTT of cancer. *Colloids Surf B Biointerf.* (2020) 186:110701. doi: 10.1016/j.colsurfb.2019.110701
- 30. Ide MS, Davis RJ. The important role of hydroxyl on oxidation catalysis by gold nanoparticles. Accounts Chem Res. (2014) 47:825-33. doi: 10.1021/ar4001907
- 31. Zhang R, Gao Y, Wang S, Pan J, Geng S, Li Z. Detection ofmiRNA-378based on a catalytic hairpin self-assembly reaction combined with gold nanoparticle colorimetry. *Nanotechnology.* (2024) 35. doi: 10.1088/1361-6528/ad5297
- 32. Kim H, Park M, Hwang J, Kim JH, Chung DR, Lee KS. Development of label-free colorimetric assay for MERS-CoV using gold nanoparticles. ACS Sens. (2019) 4:1306–12. doi: 10.1021/acssensors.9b00175
- 33. Appidi T, Mudigunda SV, Kodandapani S, Rengan AK. Development of label-free gold nanoparticle based rapid colorimetric assay for clinical/point-of-care screening of cervical cancer. *Nanoscale Adv.* (2020) 2:5737–45. doi: 10.1039/d0na00686f
- 34. Appidi T, Vakada M, Buddhiraju HS, Chinchulkar SA, Kota A, Yadav DN. Development of a point-of-care cervico-vaginal sampling/testing device for the colorimetric detection of cervical cancer. *Diagnost (Basel)*. (2023) 13:1382. doi: 10.3390/diagnostics13081382
- 35. Perkins RB, Wentzensen N, Guido RS, Schiffman M. Cervical cancer screening: A review. *JAMA*. (2023) 330:547–58. doi: 10.1001/jama.2023.13174
- 36. Xiao H, Chen W, Lin M, Jiang S, Cui X, Zhao S. Rapid immunoassay for dual-mode detection of HPV16 and HPV18 DNA based on Au@PdPt nanoparticles. *Anal Methods.* (2024) 16:1862–9. doi: 10.1039/d3ay02307a
- 37. Navarro Chica CE, Alfonso Tobón LL, López Abella JJ, Valencia Piedrahita MP, Neira Acevedo D, Bermúdez PC. Nanoparticle-based colorimetric assays for early and rapid screening of the oncogenic HPV variants 16 and 18. *Clin Chim Acta.* (2025) 568:120144. doi: 10.1016/j.cca.2025.120144

- 38. Weng J, Sheng N, Wang R, Liang S, Wang C, Bai X. Multiplex visualized closed-tube PCR with hamming distance 2 code for 15 HPV subtype typing. *Anal Chem.* (2021) 93:5529–36. doi: 10.1021/acs.analchem.1c00035
- 39. Yang Y, Qing Y, Hao X, Fang C, Ouyang P, Li H. APTES-modified remote self-assembled DNA-based electrochemical biosensor for human papillomavirus DNA detection. *Biosens (Basel)*. (2022) 12:449. doi: 10.3390/bios12070449
- 40. Kuntamung K, Sangthong P, Jakmunee J, Ounnunkad K. Simultaneous immunodetection of multiple cervical cancer biomarkers based on a signal-amplifying redox probes/polyethyleneimine-coated gold nanoparticles/2D tungsten disulfide/graphene oxide nanocomposite platform. *Bioelectrochemistry*. (2024) 160:108780. doi: 10.1016/j.bioelechem.2024.108780
- 41. Su S, Sun Q, Ma J, Zhu D, Wang F, Chao J. Ultrasensitive analysis of microRNAs with gold nanoparticle-decorated molybdenum disulfide nanohybrid-based multilayer nanoprobes. *Chem Commun (Camb)*. (2020) 56:9012–5. doi: 10.1039/d0cc03845h
- 42. Zhang JX, Lv CL, Tang C, Jiang LY, Wang AJ, Feng JJ. Ultrasensitive sandwich-typed electrochemical immunoassay for detection of squamous cell carcinoma antigen based on highly branched PtCo nanocrystals and dendritic mesoporous SiO2@AuPt nanoparticles. *Mikrochim Acta*. (2022) 189:416. doi: 10.1007/s00604-022-05520-1
- 43. Kotal H, Kalyani T, Lala A, R K, Mandal RK, Jana SK. Development of a highly sensitive, label-free electrochemical immunosensor for p16INK4a detection: a step toward early cervical cancer diagnosis. *Anal Methods.* (2025) 17:4556–65. doi: 10.1039/d5ay00411j
- 44. Zamudio Cañas R, Jaramillo Flores ME, Vallejo Ruiz V, Delgado Macuil RJ, López Gayou V. Detection of sialic acid to differentiate cervical cancer cell lines using a Sambucus nigra lectin biosensor. *Biosens (Basel)*. (2024) 14:34. doi: 10.3390/bios14010034
- 45. Saleh MA, Zangeneh FZ, Borghei YS, Samadikhah HR, Nikkhah M, Hosseinkhani S. Detection of HPV-16 by a simple and cost-effective DNA probe: polyadenine-polythymine-decorated gold nanoparticles (PolyA-polyT@AuNPs). *Biotechnol Appl Biochem.* (2025), e2772. doi: 10.1002/bab.2772
- 46. Yang Y, Liao Y, Qing Y, Li H, Du J. Electrochemical DNA biosensors with dual-signal amplification strategy for highly sensitive HPV 16 detection. *Sens (Basel)*. (2023) 23:7380. doi: 10.3390/s23177380
- 47. Mahmoodi P, Rezayi M, Rasouli E, Avan A, Gholami M, Ghayour Mobarhan M. Early-stage cervical cancer diagnosis based on an ultra-sensitive electrochemical DNA nanobiosensor for HPV-18 detection in real samples. *J Nanobiotechnol.* (2020) 18:11. doi: 10.1186/s12951-020-0577-9
- 48. Yang N, Liu P, Cai C, Zhang R, Sang K, Shen P. Triple signal amplification strategy for the ultrasensitive electrochemical detection of human papillomavirus 16 E6/E7 mRNA. *Enzyme Microb Technol*. (2021) 149:109855. doi: 10.1016/j.enzmictec.2021.109855
- 49. Jaapar FN, Parmin NA, Halim NHA, Hashim U, Gopinath SCB, Halim FS. Micro-interdigitated electrodes genosensor based on Au-deposited nanoparticles for early detection of cervical cancer. *Int J Biol Macromol.* (2023) 253:126745. doi: 10.1016/j.ijbiomac.2023.126745
- 50. Shahdeo D, Kesarwani V, Suhag D, Ahmed J, Alshehri SM, Gandhi S. Self-assembled chitosan polymer intercalating peptide functionalized gold nanoparticles as nanoprobe for efficient imaging of urokinase plasminogen activator receptor in cancer diagnostics. *Carbohydr Polym.* (2021) 266:118138. doi: 10.1016/j.carbpol.2021.118138
- 51. Avelino KYPS, Oliveira LS, Lucena-Silva N, de Melo CP, Andrade CAS, Oliveira MDL. Metal-polymer hybrid nanomaterial for impedimetric detection of human papillomavirus in cervical specimens. *J Pharm BioMed Anal.* (2020) 185:113249. doi: 10.1016/j.jpba.2020.113249
- 52. Sun Y, Liu J, Peng X, Zhang G, Li Y. A novel photoelectrochemical array platform for ultrasensitive multiplex detection and subtype identification of HPV genes. *Biosens Bioelectron.* (2023) 224:115059. doi: 10.1016/j.bios.2023.115059
- 53. Li L, Tian H, Wang G, Ren S, Ma T, Wang Y. Ready-to-use interactive dual-readout differential lateral flow biosensor for two genotypes of human papillomavirus. *Biosens Bioelectron.* (2023) 228:115224. doi: 10.1016/j.bios.2023.115224
- 54. Hu J, Yu Y, Pan X, Han Y, She X, Liu X. Highly sensitive and specific detection of human papillomavirus type 16 using CRISPR/Cas12a assay coupled with an enhanced single nanoparticle dark-field microscopy imaging technique. *Talanta*. (2024) 278:126449. doi: 10.1016/j.talanta.2024.126449
- 55. Lu D, Ran M, Liu Y, Xia J, Bi L, Cao X. SERS spectroscopy using Au-Ag nanoshuttles and hydrophobic paper-based Au nanoflower substrate for simultaneous detection of dual cervical cancer-associated serum biomarkers. *Anal Bioanal Chem.* (2020) 412:7099–112. doi: 10.1007/s00216-020-02843-x
- 56. Panikar SS, Banu N, Haramati J, Gutierrez-Silerio GY, Bastidas-Ramirez BE, Tellez-Bañuelos MC. Anti-fouling SERS-based immunosensor for point-of-care detection of the B7-H6 tumor biomarker in cervical cancer patient serum. *Anal Chim Acta*. (2020) 1138:110–22. doi: 10.1016/j.aca.2020.09.019
- 57. Ge S, Ran M, Mao Y, Sun Y, Zhou X, Li L. A novel DNA biosensor for the ultrasensitive detection of DNA methyltransferase activity based on a high-density "hot spot" SERS substrate and rolling circle amplification strategy. *Analyst.* (2021) 146:5326–36. doi: 10.1039/d1an01034d
- 58. Gu Y, Li Z, Ge S, Mao Y, Gu Y, Cao X. A microfluidic chip using Au@SiO2 array-based highly SERS-active substrates for ultrasensitive detection of dual cervical cancer-related biomarkers. *Anal Bioanal Chem.* (2022) 414:7659–73. doi: 10.1007/s00216-022-04296-w

- 59. Karunakaran V, Saritha VNS, Ramya AN, Murali VP, Raghu KG, Sujathan K. Elucidating raman image-guided differential recognition of clinically confirmed grades of cervical exfoliated cells by dual biomarker-appended SERS-tag. *Anal Chem.* (2021) 93:11140–50. doi: 10.1021/acs.analchem.1c01607
- 60. Li Y, Jiang L, Yu Z, Jiang C, Zhang F, Jin S. SPRi/SERS dual-mode biosensor based on ployA-DNA/miRNA/AuNPs-enhanced probe sandwich structure for the detection of multiple miRNA biomarkers. *Spectrochim Acta A Mol Biomol Spectrosc.* (2024) 308:123664. doi: 10.1016/j.saa.2023.123664
- 61. Karunakaran V, Saritha VNS, Joseph MM, Nair JB, Saranya G, Raghu KG. Diagnostic spectro-cytology revealing differential recognition of cervical cancer lesions by label-free surface enhanced Raman fingerprints and chemometrics. *Nanomednanotechnol.* (2020) 29:102276. doi: 10.1016/j.nano.2020.102276
- 62. Diao X, Li X, Hou S, Li H, Qi G, Jin Y. Machine learning-based label-free SERS profiling of exosomes for accurate fuzzy diagnosis of cancer and dynamic monitoring of drug therapeutic processes. *Anal Chem.* (2023) 95:7552–9. doi: 10.1021/acs.analchem.3c00026
- 63. Li H, Wang Q, Tang J, Gao NN, Yue XX, Zhong FR. Establishment of a reliable scheme for obtaining highly stable SERS signal of biological serum. *Biosens Bioelectron*. (2021) 189:113315. doi: 10.1016/j.bios.2021.113315
- 64. Diao X, Qi G, Tian Y, Li J, Jin Y. Gap-plasmon metasurface combined with biobarcode of CD63 nanoflares for SERS detection of cancerous exosomes. *Anal Chem.* (2025) 97:13958–64. doi: 10.1021/acs.analchem.5c02115
- 65. Yin HQ, Shao G, Gan F, Ye G. One-step, rapid and green synthesis of multifunctional gold nanoparticles for tumor-targeted imaging and therapy. *Nanoscale Res Lett.* (2020) 15:29. doi: 10.1186/s11671-019-3232-3
- 66. Yim MS, Hwang YS, Bang JK, Jung DW, Kim JM, Yi GR. Morphologically homogeneous, pH-responsive gold nanoparticles for non-invasive imaging of HeLa cancer. *Nanomedicine*. (2021) 34:102394. doi: 10.1016/j.nano.2021.102394
- 67. Zhang W, Lu Y, Zang Y, Han J, Xiong Q, Xiong J. Photodynamic therapy and multi-modality imaging of up-conversion nanomaterial doped with AuNPs. *Int J Mol Sci.* (2022) 23:1227. doi: 10.3390/ijms23031227
- 68. Wang J, Huang M, Li MX, Zhu F, Cheng R, Liu JJ. The restructure of Au@Ag nanorods for cell imaging with dark-field microscope. *Talanta*. (2022) 244:123403. doi: 10.1016/j.talanta.2022.123403
- 69. Yücel O, Şengelen A, Emik S, Önay-Uçar E, Arda N, Gürdağ G. Folic acid-modified methotrexate-conjugated gold nanoparticles as nano-sized trojans for drug delivery to folate receptor-positive cancer cells. *Nanotechnology.* (2020) 31:355101. doi: 10.1088/1361-6528/ab9395
- 70. Velhal K, Sah PM, Naik HS, Raut R, Patil S, Yamgar R. Synergistic nanoformulation: streamlined one-pot synthesis enhances paclitaxel functionalization gold nanoparticles for potent anticancer activity. *Cell Biochem Biophys.* (2025). doi: 10.1007/s12013-025-01701-w
- 71. Matić IZ, Mraković A, Rakočević Z, Stoiljković M, Pavlović VB, Momić T. Anticancer effect of novel luteolin capped gold nanoparticles selectively cytotoxic towards human cervical adenocarcinoma HeLa cells: An *in vitro* approach. *J Trace Elem Med Biol.* (2023) 80:127286. doi: 10.1016/j.jtemb.2023.127286
- 72. Lopes-Nunes J, Agonia AS, Rosado T, Gallardo E, Palmeira-de-Oliveira R, Palmeira-de-Oliveira A. Aptamer-functionalized gold nanoparticles for drug delivery to gynecological carcinoma cells. *Cancers (Basel)*. (2021) 13:4038. doi: 10.3390/cancers13164038
- 73. Farooq MU, Dovzhenko AP, Zairov RR, Abyzbekova G, Harb M, Arkook B. Insights into the engineered gold nanoparticle-based remedy for supplementation therapy of ovarian carcinoma. *ACS Omega.* (2024) 9:33033–43. doi: 10.1021/acsomega.4c04134
- 74. Fathy MM, Elfiky AA, Bashandy YS, Hamdy MM, Elgharib AM, Ibrahim IM. An insight into synthesis and antitumor activity of citrate and gallate stabilizing gold nanospheres. *Sci Rep-uk.* (2023) 13:2749. doi: 10.1038/s41598-023-29821-4
- 75. Srinivas Naik L, Devi CVR. Induction of extrinsic and intrinsic apoptosis in cervical cancer cells by Momordica dioica mediated gold nanoparticles. *IET Nanobiotechnol.* (2020) 14:172–9. doi: 10.1049/iet-nbt.2019.0075
- 76. Prasad A, Khatua A, Mohanta YK, Saravanan M, Meena R, Ghosh I. Low-dose exposure to phytosynthesized gold nanoparticles combined with glutamine deprivation enhances cell death in the cancer cell line HeLa via oxidative stress-mediated mitochondrial dysfunction and G0/G1 cell cycle arrest. *Nanoscale*. (2022) 14:10399–417. doi: 10.1039/d2nr02150a
- 77. Kamil Shareef NA, Zandsalimi F, Tavoosidana G. Gold nanoparticles (AuNPs) decrease the viability of cervical cancer cells by inducing the BAX gene and activating antioxidant enzymes. *Mol Biol Rep.* (2024) 51:287. doi: 10.1007/s11033-024-09253-7
- 78. Jung DW, Ro HJ, Kim J, Kim SI, Yi GR, Lee G. Biophysical restriction of growth area using a monodispersed gold sphere nanobarrier prolongs the mitotic phase in HeLa cells. $RSC\ Adv.\ (2019)\ 9:37497-506.$ doi: 10.1039/c9ra08410j
- 79. Liu P, Wang Y, Liu Y, Tan F, Li J, Li N. S-nitrosothiols loaded mini-sized Au@ silica nanorod elicits collagen depletion and mitochondrial damage in solid tumor treatment. *Theranostics*. (2020) 10:6774–89. doi: 10.7150/thno.42661
- 80. Imanparast A, Attaran N, Eshghi H, Sazgarnia A. Surface modification of gold nanoparticles with 6-mercapto-1-hexanol to facilitate dual conjugation of protoporphyrin IX and folic acid for improving the targeted photochemical internalization. *Iran J Basic Med Sci.* (2022) 25:970–9. doi: 10.22038/IJBMS.2022.63622.14033

- 81. Teixeira ARC, Antunes J, Pinto CIG, Cabral Campello MP, Santos P, Gomes CéM. GRPR-targeted gold nanoparticles as selective radiotherapy enhancers in glioblastoma. *Phys Med Biol.* (2025) 70. doi: 10.1088/1361-6560/ade222
- 82. Liu J, Liang Y, Liu T, Li D, Yang X. Anti-EGFR-conjugated hollow gold nanospheres enhance radiocytotoxic targeting of cervical cancer at megavoltage radiation energies. *Nanoscale Res Lett.* (2015) 10:218. doi: 10.1186/s11671-015-0923-2
- 83. Amani S, Mehdizadeh A, Movahedi MM, Keshavarz M, Koosha F. Investigation of the dose-Enhancement effects of spherical and rod-Shaped gold nanoparticles on the HeLa cell line. *Galen Med J.* (2020) 4:e1581. doi: 10.31661/gmj.v9i0.1581
- 84. Gray TM, David S, Bassiri N, Patel DY, Kirby N, Mayer KM. Microdosimetric and radiobiological effects of gold nanoparticles at therapeutic radiation energies. *Int J Radiat Biol.* (2023) 99:308–17. doi: 10.1080/09553002.2022.2087931
- 85. Aydindogan E, Ceylan AE, Timur S. Paper-based colorimetric spot test utilizing smartphone sensing for detection of biomarkers. *Talanta*. (2020) 208:120446. doi: 10.1016/j.talanta.2019.120446
- 86. Liu H, Wu MX, Ding SN. High-density gold nanoparticles implanted on Mg/Fe LDH nanoflowers assisted lateral flow immuno-dipstick assay for visual detection of human epididymal protein 4. *Biosens (Basel)*. (2022) 12:797. doi: 10.3390/bios12100797
- 87. Ibadi I, Naseri A, Khalilzadeh B. Development of an electrochemical biosensor based on MOF@AuNPs nanocomposite for early-stage evaluation of ovarian cancer via CA125 oncomarker in human serum samples. *Sens Bio Sens Res.* (2025) 49:100838. doi: 10.1016/j.sbsr.2025.100838
- 88. Gharehaghaji ZH, Khalilzadeh B, Yousefi H, Mohammad-Rezaei R. An electrochemical immunosensor based on MXene-GQD/AuNPs for the detection of trace amounts of CA-125 as specific tracer of ovarian cancer. *Mikrochim Acta.* (2024) 191:418. doi: 10.1007/s00604-024-06469-z
- 89. Shen R, Zhang J, Huang W, Wu S, Li G, Zou S. Dynamic light scattering and fluorescence dual-signal sensing of cancer antigen-125 via recognition of the polymerase chain reaction product with gold nanoparticle probe. *Anal Chim Acta*. (2021) 1145:87–94. doi: 10.1016/j.aca.2020.11.005
- 90. Cotchim S, Thavarungkul P, Kanatharana P, Thantipwan T, Jiraseree-Amornkun A, Wannapob R. A portable electrochemical immunosensor for ovarian cancer uses hierarchical microporous carbon material from waste coffee grounds. *Mikrochim Acta.* (2023) 190:232. doi: 10.1007/s00604-023-05798-9
- 91. Tang Y, Liu Y, Xia Y, Zhao F, Zeng B. Simultaneous detection of ovarian cancer-concerned HE4 and CA125 markers based on cu single-atom-triggered CdS QDs and Eu MOF@Isoluminol ECL. *Anal Chem.* (2023) 95:4795–802. doi: 10.1021/acs.analchem.3c00273
- 92. Samadi Pakchin P, Fathi M, Ghanbari H, Saber R, Omidi Y. A novel electrochemical immunosensor for ultrasensitive detection of CA125 in ovarian cancer. *Biosens Bioelectron*. (2020) 153:112029. doi: 10.1016/j.bios.2020.112029
- 93. Hu D, Liang H, Wang X, Luo F, Qiu B, Lin Z. Highly sensitive and selective photoelectrochemical aptasensor for cancer biomarker CA125 based on AuNPs/GaN Schottky junction. Anal Chem. (2020) 92:10114–20. doi: 10.1021/ acs.analchem.0c02117
- 94. Xu X, Ji J, Chen P, Wu J, Jin Y, Zhang L. Salt-induced gold nanoparticles aggregation lights up fluorescence of DNA-silver nanoclusters to monitor dual cancer markers carcinoembryonic antigen and carbohydrate antigen 125. *Anal Chim Acta*. (2020) 1125:41–9. doi: 10.1016/j.aca.2020.05.027
- 95. Jin W, Chen R, Wu L, Peng C, Song Y, Miao L. Tetrahedral DNA nanostructure enhanced toehold-mediated strand displacement for highly sensitive electrochemiluminescence assay of CA125. *Bioelectrochemistry*. (2024) 155:108572. doi: 10.1016/j.bioelechem.2023.108572
- 96. Amirabadizadeh M, Siampour H, Abbasian S, Nikkhah M, Moshaii A. Aptasensor for ovarian cancer biomarker detection using nanostructured gold electrodes. *Mikrochim Acta*. (2023) 191:2. doi: 10.1007/s00604-023-06072-8
- 97. Bilgi Kamaç M, Altun M, Yilmaz M, Sezgintürk MK. A label-free dual immunosensor for the simultaneous electrochemical determination of CA125 and HE4 biomarkers for the early diagnosis of ovarian cancer. *Anal Bioanal Chem.* (2023) 415:1709–18. doi: 10.1007/s00216-023-04569-y
- 98. Yılmaz M, Bilgi M. A disposable impedimetric immunosensor for the analysis of CA125 in human serum samples. *BioMed Microdevices*. (2024) 26:8. doi: 10.1007/s10544-023-00691-x
- 99. Jin W, Chen R, Wu L, Peng C, Song Y, Miao L. An "on-off" electrochemical immunosensor for the detection of the glycan antigen CA125 by amplification signals using electropositive COFs. *Talanta*. (2025) 286:127593. doi: 10.1016/j.talanta.2025.127593
- 100. Dezhakam E, Dehghani S, Faraghi Vayghan R, Naseri A, Khalilzadeh B, Isildak I. An early stage electrochemical evaluation of ovarian cancer: α-MnO2 nanorod and AuNP hybrid nanoarchitectures. *Langmuir*. (2025) 41:17573–83. doi: 10.1021/acs.langmuir.5c01178
- 101. Mu W, Wu C, Wu F, Gao H, Ren X, Feng J. Ultrasensitive and label-free electrochemical immunosensor for the detection of the ovarian cancer biomarker CA125 based on CuCo-ONSs@AuNPs nanocomposites. *J Pharm BioMed Anal.* (2024) 243:116080. doi: 10.1016/j.jpba.2024.116080
- 102. Asare-Werehene M, Hunter RA, Gerber E, Reunov A, Brine I, Chang CY, et al. The application of an extracellular vesicle-based biosensor in early diagnosis and prediction of chemoresponsiveness in ovarian cancer. *Cancers.* (2023) 15:2566. doi: 10.3390/cancers15092566

- 103. Samanci SN, Ozcelikay-Akyildiz G, Bellur Atici E, Ozkan SA. Advanced sensor technologies for niraparib detection: A comparative study of molecularly imprinted polymer and nanosensor systems. *Talanta*. (2025) 294:128205. doi: 10.1016/j.talanta.2025.128205
- 104. Kang Y, Masud MK, Guo Y, Zhao Y, Nishat ZS, Zhao J. Au-loaded superparamagnetic mesoporous bimetallic CoFeB nanovehicles for sensitive autoantibody detection. ACS Nano. (2023) 17:3346–57. doi: 10.1021/acsnano.2c07694
- 105. Chen D, Wu Y, Tilley RD, Gooding JJ. Rapid and ultrasensitive electrochemical detection of DNA methylation for ovarian cancer diagnosis. *Biosens Bioelectron*. (2022) 206:114126. doi: 10.1016/j.bios.2022.114126
- 106. Liu X, Wang Q, Chen J, Chen X, Yang W. Ultrasensitive electrochemiluminescence biosensor for the detection of tumor exosomes based on peptide recognition and luminol-AuNPs@g-C3N4 nanoprobe signal amplification. *Talanta*. (2021) 221:121379. doi: 10.1016/j.talanta.2020.121379
- 107. Xu X, Tang L, Yu Y, Zhang J, Zhou X, Zhou T. Cooperative amplification of PRussian blue as a signal indicator and functionalized metal-organic framework-based electrochemical biosensor for an ultrasensitive HE4 assay. *Biosens Bioelectron.* (2024) 262:116541. doi: 10.1016/j.bios.2024.116541
- 108. Rockett TW, Almahyawi M, Ghimire ML, Jonnalagadda A, Tagliaferro V, Seashols-Williams SJ. Cluster-enhanced nanopore sensing of ovarian cancer marker peptides in urine. ACS Sens. (2024) 9:860–9. doi: 10.1021/acssensors.3c02207
- 109. Beffara F, Perumal J, Mahyuddin AP, Choolani M, Khan SA, Auguste JL. Development of highly reliable SERS-active photonic crystal fiber probe and its application in the detection of ovarian cancer biomarker in cyst fluid. *J Biophotonics*. (2020) 13:e201960120. doi: 10.1002/jbio.201960120
- 110. Kahn N, Lavie O, Paz M, Segev Y, Haick H. Dynamic nanoparticle-based flexible sensors: diagnosis of ovarian carcinoma from exhaled breath. *Nano Lett.* (2015) 15:7023–8. doi: 10.1021/acs.nanolett.5b03052
- 111. Kumar D, Sakhare N, Das S, Kale P, Mathur A, Mirapurkar S. Development of technetium-99m labeled ultrafine gold nanobioconjugates for targeted imaging of folate receptor positive cancers. *Nucl Med Biol.* (2021) 93:1–10. doi: 10.1016/j.nucmedbio.2020.11.001
- 112. Beik J, Alamzadeh Z, Mirrahimi M, Sarikhani A, Shakerian Ardakani T, Asadi MR. Multifunctional theranostic graphene oxide nanoflakes as MR imaging agents with enhanced photothermal and radiosensitizing properties. *ACS Appl Bio Mater.* (2021) 4:4280–91. doi: 10.1021/acsabm.1c00104
- 113. Kumar D, Moghiseh M, Chitcholtan K, Mutreja I, Lowe C, Kaushik A. LHRH conjugated gold nanoparticles assisted efficient ovarian cancer targeting evaluated via spectral photon-counting CT imaging: a proof-of-concept research. *J Mater Chem B*. (2023) 11:1916–28. doi: 10.1039/d2tb02416k
- 114. Hada AM, Craciun AM, Focsan M, Borlan R, Soritau O, Todea M. Folic acid functionalized gold nanoclusters for enabling targeted fluorescence imaging of human ovarian cancer cells. *Talanta*. (2021) 225:121960. doi: 10.1016/j.talanta.2020.121960
- 115. Taheri-Ledari R, Zhang W, Radmanesh M, Cathcart N, Maleki A, Kitaev V. Plasmonic photothermal release of docetaxel by gold nanoparticles incorporated onto halloysite nanotubes with conjugated 2D8-E3 antibodies for selective cancer therapy. *J Nanobiotechnol.* (2021) 19:239. doi: 10.1186/s12951-021-00982-6
- 116. Verdin A, Malherbe C, Müller WH, Bertrand V, Eppe G. Multiplex micro-SERS imaging of cancer-related markers in cells and tissues using poly(allylamine)-coated Au@Ag nanoprobes. *Anal Bioanal Chem.* (2020) 412:7739–55. doi: 10.1007/s00216-020-02927-8
- 117. Honda K, Hish T. On-tissue polysulfide visualization by surface-enhanced Raman spectroscopy benefits patients with ovarian cancer to predict post-operative chemosensitivity. *Redox Biol.* (2021) 41:101926. doi: 10.1016/j.redox.2021.101926
- 118. Lee CS, Kim TW, Oh DE, Bae SO, Ryu J, Kong H. *In vivo* and *in vitro* anticancer activity of doxorubicin-loaded DNA-AuNP nanocarrier for the ovarian cancer treatment. *Cancers (Basel).* (2020) 12:634. doi: 10.3390/cancers12030634
- 119. Hossen MN, Wang L, Chinthalapally HR, Robertson JD, Fung KM, Wilhelm S. Switching the intracellular pathway and enhancing the therapeutic efficacy of small interfering RNA by auroliposome. *Sci Adv.* (2020) 6:eaba5379. doi: 10.1126/sciadv.aba5379
- 120. Jabir M, Sahib UI, Taqi Z, Taha A, Sulaiman G, Albukhaty S. Linalool-loaded glutathione-modified gold nanoparticles conjugated with CALNN peptide as apoptosis inducer and NF-κB translocation inhibitor in SKOV-3 cell line. *Int J Nanomed.* (2020) 15:9025–47. doi: 10.2147/IJN.S276714
- 121. Tunc CU, Kursunluoglu G, Akdeniz M, Kutlu AU, Han MI, Yerer MB. Investigation of gold nanoparticle naproxen-derived conjugations in ovarian cancer. *ACS Mater Au.* (2023) 3:483–91. doi: 10.1021/acsmaterialsau.3c00033
- 122. Salas-Huenuleo E, Hernández A, Lobos-González L, Polakovičová I, Morales-Zavala F, Araya E. Peptide targeted gold nanoplatform carrying miR-145 induces antitumoral effects in ovarian cancer cells. *Pharmaceutics*. (2022) 14:958. doi: 10.3390/pharmaceutics14050958
- 123. Wang Z, Zhao Y, Yang Z, Li X, Xing H, Qu W. Construction of intelligent responsive drug delivery system and multi-mode imaging based on gold nanodots. *Macromol Rapid Commun.* (2022) 43:e2200034. doi: 10.1002/marc.202200034
- 124. Piktel E, Oscilowska I, Suprewicz Ł, Depciuch J, Marcińczyk N, Chabielska E. Peanut-shaped gold nanoparticles with shells of ceragenin CSA-131 display the ability

- to inhibit ovarian cancer growth in vitro and in a tumor xenograft model. Cancers (Basel), (2021) 13:5424, doi: 10.3390/cancers13215424
- 125. Maity R, Chatterjee M, Banerjee A, Das A, Mishra R, Mazumder S. Gold nanoparticle-assisted enhancement in the anti-cancer properties of theaflavin against human ovarian cancer cells. *Mater Sci Eng C Mater Biol Appl.* (2019) 104:109909. doi: 10.1016/j.msec.2019.109909
- 126. Salamone TA, Marotta S, Mrmić S, Raffa S, Cerra S, Pennacchi B. MiR-200c synergizes with trastuzumab-loaded gold nanoparticles to overcome resistance in ovarian cancer cells. *Cancer Nanotechnol.* (2025) 16:29. doi: 10.1186/s12645-025-00330-5
- 127. Torres J, Calderón-Montaño JM, Prieto-Dapena F, López-Lázaro M, Rueda M, Rabasco-Álvarez AM. A quality-by-design approach for optimizing the functionalization of gold nanoparticles onto the surface of doxorubicin-encapsulated liposomes. *Int J Pharm.* (2025) 669:125040. doi: 10.1016/j.ijpharm.2024.125040
- 128. Wang X, Xiong T, Cui M, Li N, Li Q, Zhu L. A novel targeted co-delivery nanosystem for enhanced ovarian cancer treatment via multidrug resistance reversion and mTOR-mediated signaling pathway. *J Nanobiotechnol.* (2021) 19:444. doi: 10.1186/s12951-021-01139-1
- 129. Kip B, Tunc CU, Aydin O. Triple-combination therapy assisted with ultrasound-active gold nanoparticles and ultrasound therapy against 3D cisplatin-resistant ovarian cancer model. *Ultrason Sonochem.* (2022) 82:105903. doi: 10.1016/iultsonch.2021.105903
- 130. Arvizo RR, Saha S, Wang E, Robertson JD, Bhattacharya R, Mukherjee P. Inhibition of tumor growth and metastasis by a self-therapeutic nanoparticle. *Proc Natl Acad Sci U S A.* (2013) 110:6700–5. doi: 10.1073/pnas.1214547110
- 131. Hossen MN, Wang L, Dwivedi SKD, Zhang Y, Rao G, Elechalwar CK. Gold nanoparticles disrupt the IGFBP2/mTOR/PTEN axis to inhibit ovarian cancer growth. *Adv Sci (Weinh)*. (2022) 9:e2200491. doi: 10.1002/advs.202200491
- 132. Zhang Y, Elechalawar CK, Yang W, Frickenstein AN, Asfa S, Fung KM. Disabling partners in crime: Gold nanoparticles disrupt multicellular communications within the tumor microenvironment to inhibit ovarian tumor aggressiveness. *Mater Today* (*Kidlington*). (2022) 56:79–95. doi: 10.1016/j.mattod.2022.01.025
- 133. Zhang Y, Elechalwar CK, Hossen MN, Francek ER, Dey A, Wilhelm S. Gold nanoparticles inhibit activation of cancer-associated fibroblasts by disrupting communication from tumor and microenvironmental cells. *Bioact Mater.* (2021) 6:326–32. doi: 10.1016/j.bioactmat.2020.08.009
- 134. Zhang Y, Xiong X, Huai Y, Dey A, Hossen MN, Roy RV. Gold nanoparticles disrupt tumor microenvironment endothelial cell cross talk to inhibit angiogenic phenotypes *in vitro. Bioconjug Chem.* (2019) 30:1724–33. doi: 10.1021/acs.bioconjchem.9b00262
- 135. Zhang M, Zheng H, Zhu X, Liu S, Jin H, Chen Y. Synchronously evoking disulfidptosis and ferroptosis via systematical glucose deprivation targeting SLC7A11/GSH/GPX4 antioxidant axis. *ACS Nano*. (2025) 19:14233–48. doi: 10.1021/acsnano.5c00730
- 136. Ali MRK, Wu Y, Ghosh D, Do BH, Chen K, Dawson MR. Nuclear membrane-targeted gold nanoparticles inhibit cancer cell migration and invasion. ACS Nano. (2017) 11:3716-26. doi: 10.1021/acsnano.6b08345
- 137. Asl SS, Tafvizi F, Noorbazargan H. Biogenic synthesis of gold nanoparticles using Satureja rechingeri Jamzad: a potential anticancer agent against cisplatin-resistant A2780CP ovarian cancer cells. *Environ Sci pollut Res Int.* (2023) 30:20168–84. doi: 10.1007/s11356-022-23507-6
- 138. Piktel E, Ościłowska I, Suprewicz Ł, Depciuch J, Marcińczyk N, Chabielska E. ROS-mediated apoptosis and autophagy in ovarian cancer cells treated with peanutshaped gold nanoparticles. *Int J Nanomed.* (2021) 16:1993–2011. doi: 10.2147/INS.277014
- 139. Malik IS, Nair NK, B A, Mishra S, Unnithan S, Narayana C. Optimizing branch morphology in gold nanostars to improve HER2-targeted cytotoxicity in HER2-overexpressing cancer cells in the presence of serum proteins. *Langmuir*. (2025) 41:15796–804. doi: 10.1021/acs.langmuir.5c00350
- 140. Wei Q, Arami H, Santos HÁ, Zhang H, Li Y, He J. Intraoperative assessment and photothermal ablation of the tumor margins using gold nanoparticles. *Adv Sci (Weinh)*. (2021) 8:2002788. doi: 10.1002/advs.202002788
- 141. Shen Y, Wang M, Wang H, Zhou J, Chen J. Multifunctional human serum albumin fusion protein as a docetaxel nanocarrier for chemo-photothermal synergetic therapy of ovarian cancer. ACS Appl Mater Interf. (2022) 14:19907–17. doi: 10.1021/acsami.2c03687
- 142. Wang Z, Sun X, Huang T, Song J, Wang Y. A sandwich nanostructure of gold nanoparticle coated reduced graphene oxide for photoacoustic imaging-guided photothermal therapy in the second NIR window. *Front Bioeng Biotech.* (2020) 8:655. doi: 10.3389/fbioe.2020.00655
- 143. Choe HS, Shin MJ, Kwon SG, Lee H, Kim DK, Choi KU. Yolk-shell-type gold nanoaggregates for chemo- and photothermal combination therapy for drug-resistant cancers. ACS Appl Mater Interf. (2021) 13:53519–29. doi: 10.1021/acsami.1c10036
- 144. Rokhgireh S, Chaichian S, Mehdizadeh Kashi A, Haji Ali B, Tehermanesh K, Ajdary M. Curcumin-gold nanoshell mediated near-infrared irradiation on human ovarian cancer cell: *in vitro* study. *Med Oncol.* (2025) 42:145. doi: 10.1007/s12032-025-02687-4

- 145. Zhao J, Tu K, Liu Y, Qin Y, Wang X, Qi L. Photo-controlled aptamers delivery by dual surface gold-magnetic nanoparticles for targeted cancer therapy. *Mater Sci Eng C Mater Biol Appl.* (2017) 80:88–92. doi: 10.1016/j.msec.2017.04.044
- 146. Liu A, Li L, Wang Z, Li X, Liang H, Yang J. Ultrasmall Au-GRHa nanosystem for FL/CT dual-mode imaging-guided targeting photothermal therapy of ovarian cancer. *Anal Chem.* (2025) 97:2232–43. doi: 10.1021/acs.analchem.4c05320
- 147. Ma X, Zhou W, Zhang R, Zhang C, Yan J, Feng J. Minimally invasive injection of biomimetic Nano@Microgel for in *situ* ovarian cancer treatment through enhanced photodynamic reactions and photothermal combined therapy. *Mater Today Bio*. (2023) 20:100663. doi: 10.1016/j.mtbio.2023.100663
- 148. Geng F, Song K, Xing JZ, Yuan C, Yan S, Yang Q. Thio-glucose bound gold nanoparticles enhance radio-cytotoxic targeting of ovarian cancer. *Nanotechnology*. (2011) 22:285101. doi: 10.1088/0957-4484/22/28/285101
- 149. Żelechowska-Matysiak K, Wawrowicz K, Wierzbicki M, Budlewski T, Bilewicz A, Majkowska-Pilip A. Radiobioconjugate of kadcyla with radioactive gold nanoparticles for targeted therapy of HER2-overexpressing cancers. *Mol Pharmaceut*. (2025) 22:4019–31. doi: 10.1021/acs.molpharmaceut.5c00288
- 150. McDougall RM, Cahill HF, Power ME, MacCormack TJ, Meli MV, Rourke JL. Multiparametric cytotoxicity assessment: the effect of gold nanoparticle ligand functionalization on SKOV3 ovarian carcinoma cell death. *Nanotoxicology*. (2022) 16:355–74. doi: 10.1080/17435390.2022.2095312
- 151. Baran MF, Keskin C, Baran A, Eftekhari A, Omarova S, Khalilov R. The investigation of the chemical composition and applicability of gold nanoparticles synthesized with amygdalus communis (Almond) leaf aqueous extract as antimicrobial and anticancer agents. *Molecules*. (2023) 28:2428. doi: 10.3390/molecules28062428
- 152. Sani A, Cao C, Cui D. Toxicity of gold nanoparticles (AuNPs): A review. Biochem Biophys Rep. (2021) 26:100991. doi: 10.1016/j.bbrep.2021.100991
- 153. Poley M, Mora-Raimundo P, Shammai Y, Kaduri M, Koren L, Adir O. Nanoparticles accumulate in the female reproductive system during ovulation affecting cancer treatment and fertility. ACS Nano. (2022) 16:5246–57. doi: 10.1021/acsnano.1c07237

- 154. Guo WB, Wu C, Yang L, Miao AJ. Pre-exposure to titanium or iron oxide nanoparticles suppresses the subsequent cellular uptake of gold nanoparticles. *Sci Total Environ*. (2023) 875:162491. doi: 10.1016/j.scitotenv.2023.162491
- 155. García MC, Naitlho N, Calderón-Montaño JM, Drago E, Rueda M, Longhi M. Cholesterol levels affect the performance of AuNPs-decorated thermo-sensitive liposomes as nanocarriers for controlled doxorubicin delivery. *Pharmaceutics*. (2021) 13:973. doi: 10.3390/pharmaceutics13070973
- 156. Dai Q, Wilhelm S, Ding D, Syed AM, Sindhwani S, Zhang Y. Quantifying the ligand-coated nanoparticle delivery to cancer cells in solid tumors. $ACS\ Nano.\ (2018)\ 12:8423-35.$ doi: 10.1021/acsnano.8b03900
- 157. Manivasagan P, Oh J. Production of a novel fucoidanase for the green synthesis of gold nanoparticles by streptomyces sp. and its cytotoxic effect on HeLa cells. *Mar Drugs.* (2015) 13:6818–37. doi: 10.3390/md13116818
- 158. Suh DH, Lee SJ, Kim H, Song KY, Jo JY, Chae SJ. Effect of CO2 fractional laser preTreatment in photothermal therapy using ethosome gold nanoparticles: A preliminary study. *J Cosmet Dermatol.* (2025) 24:e70349. doi: 10.1111/jocd.70349
- 159. Ramírez-Nava G, Santos-Cuevas C, Ferro-Flores G, Ocampo-García B, Chairez I, Gómez-Argumosa E. Hybrid (2D/3D) dosimetry of radiolabeled gold nanoparticles for sentinel lymph node detection in patients with breast cancer. *Contrast Media Mol Imaging.* (2020) 2020:2728134. doi: 10.1155/2020/2728134
- 160. Khoobchandani M, Katti KK, Karikachery AR, Thipe VC, Srisrimal D, Mohandoss DKD. New approaches in breast cancer therapy through green nanotechnology and nano-ayurvedic medicine pre-clinical and pilot human clinical investigations. *Int J Nanomed.* (2020) 15:181–97. doi: 10.2147/IJN.S219042
- 161. Choi YJ, Kim JS, Kim WS. Photothermal therapy using gold nanoparticles and a long-pulsed 755-nm alexandrite laser to treat facial photoaging in Asian skin: A prospective clinical trial. *Laser Surg Med.* (2022) 54:1060–70. doi: 10.1002/lsm.23581
- 162. Sazgarnia A, Shanei A, Taheri ART, Meibodi NT, Eshghi H, Attaran N. Therapeutic effects of acoustic cavitation in the presence of gold nanoparticles on a colon tumor model. *J Ultrasound Med*. (2013) 32:475–83. doi: 10.7863/jum.2013.32.3.475

Glossary

atossary			
FDA	US Food and Drug Administration	GO/SPIO/AuNP	Graphene oxide/superparamagnetic iron oxide/gold nanoparticle
PEG	Polyethylene glycol	ICP-MS	Inductively coupled plasma mass spectrometry
OCT	Optical coherence tomography	FLIM	Fluorescence lifetime imaging microscopy
VIA	Visual inspection with acetic acid	SCRM	Scanning confocal Raman microscopy
LOD	Limit of detection	FSH33	Follicle-stimulating hormone peptide fragment
LFA	Lateral flow assay	VEGF	Vascular endothelial growth factor
PDA	Polydopamine	PVA	Poly
PEBA	Photoelectrochemical biochip array	AuNCs	Gold nanoclusters
MLNPs	Multilayered nanoparticles	PDGF	Platelet-Derived Growth Factor
WS ₂	Tungsten disulfide		
MoS_2	Molybdenum disulfide	uPA	Urokinase-Type Plasminogen Activator
ND	Neutral density filter	TSP1	Thrombospondin-1
4-MBA	4-Mercaptobenzoic acid	Fe-Ap	Iron-Apigenin
DTNB	5,5'-Dithiobis-(2-nitrobenzoic acid)	AuNSs	Gold nanostructures
4,4'-DP	4,4'-Dipyridyl	HSA	Human Serum Albumin
RGD	Arginylglycylaspartic acid peptide	MMP-2	Matrix Metalloproteinase-2
NLS	Nuclear localization signal	rGO	Reduced Graphene Oxide
TAP	Tris(2-aminophenol)	aAuYS	Aggregated Gold Yolk-Shell
PHEN	1,10-Phenanthroline	Cur-AuNShs	Curcumin-Incorporated Gold Nanoshells
3-MPA	3-Mercaptopropionic acid	GnRHR	Gonadotropin-releasing Hormone Receptor
TLR7/8	Toll-like receptors 7/8	AuNDs	Gold nanodots
MPA	3-Mercaptopropionic acid	EDC	1-Ethyl-3-(3-dimethylaminopropyl)carbodiimide
MPS	3-Mercaptopropyltrimethoxysilane	NHS	N-Hydroxysuccinimide
PVP	Polyvinylpyrrolidone	Au@MSN	Gold-coated Mesoporous Silica Nanoparticles
ECM	Extracellular matrix	Ter	Terthiophene
RNS	Reactive nitrogen species	THPP	Tetrakis(4-hydroxyphenyl)porphyrin
MB	Methylene blue	GelMA	Gelatin Methacryloyl
Pp-IX	Protoporphyrin IX	sNPS	Single-Nanoparticle Sensing System
AuNRs	Gold nanorods	MutS	DNA Mismatch Repair Protein
DEF	Dose enhancement factor	EpCAM	Epithelial cell adhesion molecule
FFPE	Formalin-fixed paraffin-embedded	COF	Covalent Organic Framework
AGR2	Anterior gradient 2	Apt	Aptamer
Mg/Fe LDH	Mg/Fe-layered double hydroxide	LDI-MS	Laser Desorption/Ionization Mass Spectrometry
PAMAM	Polyamidoamine	EMS	Endometriosis
MXene	Transition metal carbide/nitride	EphB4	Ephrin type-B receptor 4
MOF	Metal-organic framework	IDEs	Interdigitated electrodes
GQD	Graphene quantum dot	CDI	1,1'-Carbonyldiimidazole
DLS	Dynamic light scattering	MWCNT	Multi-walled carbon nanotubes
TIMO ⁺ F-KB@AuNPs	Thiolated Ionic Metal-Organic Framework-KB@AuNPs	APTES	3-Aminopropyl)triethoxysilane
PB	Prussian blue	SA-HRP	Streptavidin-Horseradish Peroxidase
СоБеВ	Cobalt iron boride	GCE	Glassy carbon electrode
		ZnO NRs	Zinc Oxide Nanorods
CDDP	Cisplatin Small outre collular vesicles	ERGO	Electrochemically Reduced Graphene Oxide
sEV VOCa	Small extracellular vesicles	SPCE	Screen-Printed Carbon Electrode
VOCs	Volatile organic compounds	FTO	Fluorine-Doped Tin Oxide
HYNIC	Hydrazinonicotinamide		

TDN Tetrahedral DNA Nanostructure DSPCE Double-Screen Printed Carbon Electrode

TMSD Toehold-Mediated Strand Displacement DES Deep Eutectic Solvent

ZIF Zeolitic Imidazolate Framework CuCo-ONSs Copper-Cobalt Oxide Nanosheets

PTH/PTB Polythiophene